Mathematical Models and Methods in Applied Sciences
Vol. 31, No. 4 (2021) 753–787

DOI: 10.1142/S0218202521500184

World Scientific
www.worldscientific.com

Efficient, second-order in time, and energy stable scheme for a new hydrodynamically coupled three components volume-conserved Allen–Cahn phase-field model

Xiaofeng Yang

Department of Mathematics,
University of South Carolina,
Columbia, SC 29208, USA
xfyang@math.sc.edu

Received 15 April 2020
Revised 24 December 2020
Accepted 30 December 2020
Published 13 April 2021
Communicated by J. Xu

In this paper, we establish a new hydrodynamically coupled phase-field model for three immiscible fluid components system. The model consists of the Navier–Stokes equations and three coupled nonlinear Allen–Cahn type equations, to which we add nonlocal type Lagrange multipliers to conserve the volume of each phase accurately. To solve the model, a linear and energy stable time-marching method is constructed by combining the stabilized-Invariant Energy Quadratization (S-IEQ) approach and the projection method. The well-posedness of the scheme and its unconditional energy stability are rigorously proved. Several numerical simulations in 2D and 3D are carried out, including spinodal decomposition, dynamical deformations of a liquid lens and rising liquid drops, to validate the model and demonstrate the efficiency and energy stability of the proposed scheme, numerically.

Keywords: Second-order; phase-field; conserved Allen–Chan; three-phase; unconditional energy stability; stabilized-IEQ.

AMS Subject Classification 2020: 65N12, 65M12, 65M70

1. Introduction

The phase-field method (diffusive interface approach) had been widely applied to model and simulate the multiphase fluid flow and a variety of multiple-component materials, see Refs. 1, 3, 7, 13, 14, 17, 18, 20 and 34 and the references therein. Its essential modeling framework is to adopt a certain number of independent phase variables to label each material component and then postulate the total free energy in terms of them. For instance, the commonly-used total free energy for simulating the two-phasic fluid flow system that consists of two immiscible fluid components usually includes two parts where one is the bulk potential (double-well or logarithmic Flory–Huggins) that yields a hydrophobic contribution, and the other one

is the conformational capillary entropic term that demands a hydrophilic property. The competition between these two types of energy potentials enables the coexistence of two distinct phases in the immiscible two-phasic system. we refer to Refs. [1,8–14,16,18,19,21,22] and [25] concerning the theoretical analysis, algorithm developments and numerical simulations for the two-phasic model.

Remarkably, it is not straightforward to extend the existing works of the two-phasic model to the multi-phase scenario. For example, a modeling approach adopted in Ref. [15] is to postulate the total free energy as a simple summation of the original biphasic energy for each variable. In this way, the obtained system consists of three nonlinear coupled Cahn–Hilliard type equations of the same format where the coupling term is induced by a Lagrangian multiplier term in each equation to enforce the no-volume loss condition. However, as illustrated in Refs. [2] and [4], such a simple system is not well-posed for the *total spreading* case (some coefficient of gradient term is negative) and thus some nonphysical instabilities at interfaces may occur. To fix this problem, in Refs. [2] and [4], a sixth-order polynomial type coupling potential is added into the free energy which can ensure the system to be well-posed as long as a specific consistency condition for the surface tension parameters is satisfied. But the sixth-order polynomial potential causes more sophisticated nonlinear couplings of all three phase-field variables. The consequence is that a highly complicated, coupled and nonlinear system arrives which brings up many substantial difficulties to design efficient and stable schemes to solve it numerically. As far as the authors know, the only energy stable, linear numerical schemes with second-order accuracy are developed based on the recently developed so-called Invariant Energy Quadratization (IEQ)[36] and Scalar Auxiliary Variable (SAV)[38,39] approaches. Except for these two methods, most of the existing methods are either first-order accurate in time, or energy unstable, or highly nonlinear, or even the combinations of these features (see Refs. [2,4] and [23]).

Meanwhile, even though the three-phasic phase-field fluid flow model had been developed for more than a decade, we note almost all the numerical work (algorithm developments or simulations) were focused on the partial model (no flow-field coupled) instead of the full hydrodynamically coupled model. It is well known that when the Navier–Stokes equations are coupled into the system, a far more complicated model for algorithm developments arrives. This is because remarkably more nonlinear coupling terms between the flow field and the phase-field variables appear in addition to the stiffness issues induced by nonlinear terms. To the best of the authors knowledge, the only scheme with unconditional energy stability for solving the hydrodynamics coupled three-phasic model is developed in Ref. [23], however, their scheme is only first-order in time, and its computational cost is relatively expensive due to the nonlinear nature.

In this paper, we consider numerical approximations for solving the hydrodynamically coupled three components phase-field model. First, instead of solving the multiple coupled nonlinear fourth-order Cahn–Hilliard equations, we formulate the ternary phase-field model by using the Allen–Cahn equation. It is well known

that the second-order Allen–Cahn system is relatively easier to solve numerically in comparison with the fourth-order Cahn–Hilliard system. But an intrinsic bottleneck using the Allen–Cahn model is that the volume cannot be conserved when time evolves. To fix this issue, we modify the model by adding a nonlocal Lagrange multiplier to each of the phase equations. This term helps to maintain the original energy law and preserve the volume accurately. Second, we develop a linear scheme that can possess unconditional energy stability and second-order accuracy by combining the IEQ approach with the stabilization technique, the projection method, as well as a subtle implicit–explicit treatment. The developed method can efficiently solve the nonlinear couplings between the velocity and phase function through the nonlinear convective and stress terms. The combination of these proved efficient methods enables one to solve a linear elliptic system for the phase-field variables and the velocity field, and a Poisson equation for the pressure at each time step. We give rigorous proofs of the well-posedness of the linear system together with the energy stability, and further demonstrate the stability and accuracy numerically in simulating some classical benchmark numerical examples in 2D and 3D including the spinodal decomposition, dynamical deformations of a liquid lens and a rising liquid drop.

The rest of the paper is organized as follows. In Sec. 2, we briefly describe the hydrodynamically coupled, volume-conserved, three components Allen–Cahn phase-field model and derive its associated PDE energy dissipation law. In Sec. 3, we present the numerical scheme and prove the well-posedness of the semi-discretized linear system and its discrete energy dissipation law rigorously. In Sec. 4, we present various numerical examples to illustrate the accuracy and efficiency of the proposed schemes. Some concluding remarks are given in Sec. 5.

2. Model System

We now develop the volume-conserved, hydrodynamically coupled Allen–Cahn phase-field model for the three components fluid flows system. Let Ω be a smooth, rectangular, open bounded, connected domain in $\mathbb{R}^d$, $d = 2, 3$. Let $\phi_{i,\, i=1,2,3}$ be the ith phase-field variable which represents the volume fraction of the ith component in the fluid mixture, i.e.

$$\phi_i = \begin{cases} 1 & \text{inside the } i\text{th component,} \\ 0 & \text{outside the } i\text{th component.} \end{cases} \tag{2.1}$$

A smooth layer with the thickness ϵ is used to connect the interface between 0 and 1. Assuming the mixture being perfect (no volume leaking), thus the three unknowns ϕ_1, ϕ_2, ϕ_3 satisfy

$$\phi_1 + \phi_2 + \phi_3 = 1. \tag{2.2}$$

This is the so-called perfect mixture or hyperplane link condition, see Refs. 2,4 and 23.

Remarkably, there exist several generalizations from the two-phasic model to the three-phasic model (cf. Refs. 2–4,16 and 23). In this paper, we adopt below the total free energy developed in Refs. 2–4,23. Hence, after coupling with the hydrodynamics, the total free energy reads as

$$E(\mathbf{u},\phi_1,\phi_2,\phi_3)=\underbrace{\int_\Omega \frac{1}{2}|\mathbf{u}|^2 d\mathbf{x}}_{\text{I}}+\underbrace{\int_\Omega \frac{3\epsilon}{8}\big(\Sigma_1|\nabla\phi_1|^2+\Sigma_2|\nabla\phi_2|^2+\Sigma_3|\nabla\phi_3|^2\big)d\mathbf{x}}_{\text{II}}$$
$$+\underbrace{\int_\Omega \frac{12}{\epsilon}F(\phi_1,\phi_2,\phi_3)d\mathbf{x}}_{\text{III}}\ . \tag{2.3}$$

We give a brief introduction for all three parts of the total free energy in (2.3), I, II, and III, as follows.

Part I is the kinetic energy for the fluid where $\mathbf{u}$ is the fluid velocity. Part II is the linear gradient part in the well-known mixing energy potential for each of the phase-field variable that contributes to the hydrophilic type (tendency of mixing) of interactions between the fluid components. The coefficients $\Sigma_i, i=1,2,3$ are called the "spreading" coefficient of the phase i at the interface between phases j and k. Part III is a nonlinear potential that reads as

$$F(\phi_1,\phi_2,\phi_3)=\frac{\Sigma_1}{2}\phi_1^2(1-\phi_1)^2+\frac{\Sigma_2}{2}\phi_2^2(1-\phi_2)^2+\frac{\Sigma_3}{2}\phi_3^2(1-\phi_3)^2$$
$$+P(\phi_1,\phi_2,\phi_3), \tag{2.4}$$

where

$$P(\phi_1,\phi_2,\phi_3)=3\Lambda\phi_1^2\phi_2^2\phi_3^2, \tag{2.5}$$

and Λ is a non-negative constant. The potential F represents the hydrophobic type (tendency of separation) of interactions. The parameter $\epsilon \ll 1$ is related to the width of the interface. As a consequence of the competition between parts II and III, the equilibrium configuration will include a diffusive interface.

The parameters, σ_{ij} $(\sigma_{12},\sigma_{13},\sigma_{23})$, prescribe surface tension parameter between the different pairs of phases, for example, σ_{12} is the surface tension parameter between the fluid 1 and fluid 2. To be algebraically consistent with the two-phasic systems, σ_{ij} $(\sigma_{12},\sigma_{13},\sigma_{23})$ should verify the following conditions:

$$\Sigma_i=\sigma_{ij}+\sigma_{ik}-\sigma_{jk},\quad i=1,2,3. \tag{2.6}$$

Note Σ_i might not be always positive. If $\Sigma_i>0$, the spreading is said to be "partial", and if $\Sigma_i<0$, it is called "total".

Assuming that the fluid is incompressible and follows a generalized Fick's law that the mass flux be proportional to the gradient of the chemical potential, we can derive the following hydrodynamically coupled Allen–Cahn model based on the L^2-gradient flow approach

$$\phi_{it}+\nabla\cdot(\mathbf{u}\phi_i)=-M\frac{\mu_i}{\Sigma_i}, \tag{2.7}$$

$$\mu_i = -\frac{3}{4}\epsilon\Sigma_i\Delta\phi_i + \frac{12}{\epsilon}(f_i + \beta_L), \quad i = 1, 2, 3, \tag{2.8}$$

$$\mathbf{u}_t + \mathbf{u}\cdot\nabla\mathbf{u} - \nu\Delta\mathbf{u} + \nabla p + \sum_{i=1}^{3}\phi_i\nabla\mu_i = 0, \tag{2.9}$$

$$\nabla\cdot\mathbf{u} = 0, \tag{2.10}$$

where $\mu_i = \frac{\delta E}{\delta\phi_i}$ is the variational derivative or chemical potential, M is the mobility parameter, $f_i = \partial_i F$, p is the pressure, ν is the fluid viscosity, β_L is the Lagrange multiplier to ensure the hyperplane link condition (2.2) and it can be derived as

$$\beta_L = -\frac{1}{\Sigma_T}\left(\frac{f_1}{\Sigma_1} + \frac{f_2}{\Sigma_2} + \frac{f_3}{\Sigma_3}\right), \tag{2.11}$$

with $\Sigma_T = \frac{1}{\Sigma_1} + \frac{1}{\Sigma_2} + \frac{1}{\Sigma_3}$. We consider in this paper either of the two type boundary conditions below:

$$\text{(i)}\quad \text{all variables are periodic, or} \quad \text{(ii)}\quad \mathbf{u}|_{\partial\Omega} = \mathbf{0}, \partial_{\mathbf{n}}\phi_i|_{\partial\Omega} = 0, \quad i = 1, 2, 3, \tag{2.12}$$

where $\mathbf{n}$ is the unit outward normal on the boundary $\partial\Omega$.

However, the Allen–Cahn dynamics (2.7) does not conserve the total volume of $\int_\Omega \phi_i d\mathbf{x}$ for any i. To fix it, we modify the system (2.7)–(2.10) to the following form:

$$\phi_{it} + (\mathbf{u}\cdot\nabla)\phi_i + (\nabla\cdot\mathbf{u})\phi_i = -M\frac{\bar{\mu}_i}{\Sigma_i}, \tag{2.13}$$

$$\mu_i = -\frac{3}{4}\epsilon\Sigma_i\Delta\phi_i + \frac{12}{\epsilon}(f_i + \beta_L), \quad i = 1, 2, 3, \tag{2.14}$$

$$\mathbf{u}_t + \mathbf{u}\cdot\nabla\mathbf{u} - \nu\Delta\mathbf{u} + \nabla p - \sum_{i=1}^{3}\bar{\mu}_i\nabla\phi_i + \sum_{i=1}^{3}\nabla(\phi_i\bar{\mu}_i) = 0, \tag{2.15}$$

$$\nabla\cdot\mathbf{u} = 0, \tag{2.16}$$

with

$$\bar{\mu}_i = \mu_i - \frac{1}{|\Omega|}\int_\Omega \mu_i d\mathbf{x}. \tag{2.17}$$

Here we use a nonlocal Lagrange multiplier term in (2.13) to cancel the variance of the volume of phase i. By taking the L^2 inner product of (2.13) with 1, we obtain the volume conservation property that reads as

$$\frac{d}{dt}\int_\Omega \phi_i d\mathbf{x} = 0. \tag{2.18}$$

Meanwhile, the convective terms in (2.13) and the stress terms in (2.15) are identical to those in (2.7) and (2.9).

Remark 2.1. The system (2.13)–(2.14) is equivalent to the following two phase-field variables system

$$\begin{cases} \phi_{it} + (\mathbf{u}\cdot\nabla)\phi_i + (\nabla\cdot\mathbf{u})\phi_i = -M\dfrac{\bar{\mu}_i}{\Sigma_i}, \\ \mu_i = -\dfrac{3}{4}\epsilon\Sigma_i\Delta\phi_i + \dfrac{12}{\epsilon}(f_i+\beta_L), \quad i=1,2, \end{cases} \tag{2.19}$$

where ϕ_3 and μ_3 are given by the following explicit formula:

$$\phi_1+\phi_2+\phi_3 = 1, \tag{2.20}$$

$$\frac{\mu_1}{\Sigma_1}+\frac{\mu_2}{\Sigma_2}+\frac{\mu_3}{\Sigma_3} = 0. \tag{2.21}$$

Since the proof is quite similar to Theorem 3.1, we omit the details here.

We now show the model equations (2.13)–(2.16) follow a dissipative energy law. By taking the L^2 inner product of (2.13) with $\bar{\mu}_i$, of (2.14) with $-\phi_{it}$, of (2.15) with $\mathbf{u}$, performing integration by parts, we obtain

$$(\phi_{it},\bar{\mu}_i) + ((\mathbf{u}\cdot\nabla)\phi_i,\bar{\mu}_i) + ((\nabla\cdot\mathbf{u})\phi_i,\bar{\mu}_i) = -M\Sigma_i\left\|\frac{\bar{\mu}_i}{\Sigma_i}\right\|^2, \tag{2.22}$$

$$-(\mu_i,\phi_{it}) = -\frac{3}{8}\epsilon\Sigma_i d_t\|\nabla\phi_i\|^2 - \frac{12}{\epsilon}(f_i+\beta_L,\phi_{it}), \tag{2.23}$$

$$\frac{1}{2}d_t\|\mathbf{u}\|^2 + \nu\|\nabla\mathbf{u}\|^2 - (p,\nabla\cdot\mathbf{u}) - \sum_{i=1}^{3}(\bar{\mu}_i\nabla\phi_i,\mathbf{u}) - \sum_{i=1}^{3}(\phi_i\bar{\mu}_i,\nabla\cdot\mathbf{u}) = 0. \tag{2.24}$$

Then, by taking the summation of (2.22), (2.23), and (2.24) for $i=1,2,3$, using (2.16) for the pressure term, the equality $(\beta_L,(\phi_1+\phi_2+\phi_3)_t) = (\beta_L,(1)_t) = 0$ due to (2.20), and the equality $(\phi_{it},\bar{\mu}_i) = (\phi_{it},\mu_i)$ due to (2.18), we obtain the following identity as

$$\frac{d}{dt}E(\mathbf{u},\phi_1,\phi_2,\phi_3) = \chi, \tag{2.25}$$

where

$$\chi = -\nu\|\nabla\mathbf{u}\|^2 - M\left(\Sigma_1\left\|\frac{\bar{\mu}_1}{\Sigma_1}\right\|^2 + \Sigma_2\left\|\frac{\bar{\mu}_2}{\Sigma_2}\right\|^2 + \Sigma_3\left\|\frac{\bar{\mu}_3}{\Sigma_3}\right\|^2\right). \tag{2.26}$$

It appears that the inequality (2.25) forms like the energy dissipation law, but in fact since Σ_i may not be always positive, one still needs to show the total free energy $E(\mathbf{u},\phi_1,\phi_2,\phi_3)$ given in (2.3) is bounded from below and the energy decay rate $\chi\le 0$ which can be ensured by the following Lemmas (cf. Ref. 2).

Lemma 2.1. *For any $\xi_1+\xi_2+\xi_3=0$, there exists a constant $\underline{\Sigma}>0$ such that*

$$\Sigma_1|\xi_1|^2+\Sigma_2|\xi_2|^2+\Sigma_3|\xi_3|^2 \ge \underline{\Sigma}(|\xi_1|^2+|\xi_2|^2+|\xi_3|^2), \tag{2.27}$$

if and only if the following condition holds:

$$\Sigma_1\Sigma_2 + \Sigma_1\Sigma_3 + \Sigma_2\Sigma_3 > 0, \quad \Sigma_i + \Sigma_j > 0, \quad \forall\, i \neq j. \tag{2.28}$$

Lemma 2.2. *Let σ_{12}, σ_{13} and σ_{23} be three positive numbers and Σ_1, Σ_2 and Σ_3 defined by (2.6) (Note Σ_i might not be positive for some i). For any $\Lambda > 0$, the bulk free energy $F(\phi_1, \phi_2, \phi_3)$ defined in (2.4) is bounded from below if ϕ_1, ϕ_2, ϕ_3 is on the hyperplane $\mathcal{S}$ in 2D with $\mathcal{S} = \{\phi_1 + \phi_2 + \phi_3 = 1\}$. Furthermore, the lower bound only depends on $\Sigma_1, \Sigma_2, \Sigma_3$ and Λ.*

From Lemma 2.1, when (2.28) holds, the summation of the gradient entropy term is bounded from below since $\nabla(\phi_1 + \phi_2 + \phi_3) = 0$ by (2.20), i.e.

$$\sum_{i=1}^{3} \Sigma_i \|\nabla\phi_i\|^2 \geq \underline{\Sigma} \sum_{i=1}^{3} \|\nabla\phi_i\|^2 \geq 0. \tag{2.29}$$

Therefore, we derive $E(\mathbf{u}, \phi_1, \phi_2, \phi_3)$ is bounded from below from (2.29) and Lemma 2.2. To show the decay rate $\chi \leq 0$, from (2.21), we derive

$$\frac{\bar{\mu}_1}{\Sigma_1} + \frac{\bar{\mu}_2}{\Sigma_2} + \frac{\bar{\mu}_3}{\Sigma_3} = 0. \tag{2.30}$$

By applying Lemma 2.1, when (2.28) holds, we have

$$-\left(\Sigma_1\left\|\frac{\bar{\mu}_1}{\Sigma_1}\right\|^2 + \Sigma_2\left\|\frac{\bar{\mu}_2}{\Sigma_2}\right\|^2 + \Sigma_3\left\|\frac{\bar{\mu}_3}{\Sigma_3}\right\|^2\right) \leq -\underline{\Sigma}\left(\left\|\frac{\bar{\mu}_1}{\Sigma_1}\right\|^2 + \left\|\frac{\bar{\mu}_2}{\Sigma_2}\right\|^2 + \left\|\frac{\bar{\mu}_3}{\Sigma_3}\right\|^2\right), \tag{2.31}$$

that implies the energy decay rate $\chi \leq 0$.

Remark 2.2. The bulk part energy $F(\phi_1, \phi_2, \phi_3)$ defined in (2.4) has to be bounded from below in order to form a meaningful physical system. For partial spreading case ($\Sigma_i > 0, \forall\, i$), one can drop the six-order polynomial term by assuming $\Lambda = 0$ since $F_0(\phi_1, \phi_2, \phi_3) \geq 0$ is naturally satisfied. For the total spreading case, Λ has to be nonzero. Moreover, to ensure the non-negativity for F, Λ has to be large enough.

For 3D case, it is shown in Ref. 2 that the bulk energy F is bounded from below when $P(\phi_1, \phi_2, \phi_3)$ takes the following form:

$$P(\phi_1, \phi_2, \phi_3) = 3\Lambda\phi_1^2\phi_2^2\phi_3^2(\phi_\alpha(\phi_1) + \phi_\alpha(\phi_2) + \phi_\alpha(\phi_3)), \tag{2.32}$$

where $\phi_\alpha(x) = \frac{1}{(1+x^2)^\alpha}$ with $0 < \alpha \leq \frac{8}{17}$.

Since (2.5) is commonly used in literatures (cf. Refs. 2 and 4), we adopt it as well for convenience. Nonetheless, it will be clear that the numerical schemes we develop in this paper can deal with either (2.4) or (2.32) without any essential difficulties.

3. Numerical Schemes

Before we construct the numerical scheme to solve the model (2.13)–(2.16), we introduce some notations here. Let $\delta t > 0$ be a time step size and set $t^n = n\delta t$ for $0 \le n \le N$ with $T = N\delta t$. The L^2 inner product of any two functions $\phi(\mathbf{x})$ and $\psi(\mathbf{x})$ is denoted by $(\phi, \psi) = \int_\Omega \phi(\mathbf{x})\psi(\mathbf{x})d\mathbf{x}$, and the L^2 norm of $\phi(\mathbf{x})$ is denoted by $\|\phi\|^2 = (\phi, \phi)$. Let ψ^n be the numerical approximation to the analytic function $\psi(\cdot, t)|_{t=t^n}$.

Since we expect to develop linear type schemes, we use the IEQ approach to handle the nonlinear potential $F(\phi_1, \phi_2, \phi_3)$. The IEQ method was recently developed in Refs. 5,6,28–30,35 and 37, where its essential idea is to transform the bulk potential into a quadratic form (since the nonlinear potential is usually bounded from below) using a set of new variables. For the reformulated model, all nonlinear terms are treated semi-explicitly, which in turn yields a linear and unconditionally energy stable system. This method bypasses those typical challenges such as the justification/adjustment of convexity or implicit/explicit terms, and provides many flexibilities to treat the complicated nonlinear terms since the only request for the nonlinear potential is bounded from below. Here we give a slight modification to it by adding some stabilization terms. Remarkably, the extra added linear stabilization term is particularly effective to improve the energy stability while keeping the required accuracy. The projection method is used to discretize the Navier–Stokes equations thus the computations of the velocity can be decoupled from the pressure. For the coupled nonlinear terms like the stress and convective terms, we discretize them by using the implicit–explicit combination. The detailed procedure to develop the scheme is presented as follows:

We define an auxiliary function $U(\mathbf{x}, t)$ as

$$U = \sqrt{F(\phi_1, \phi_2, \phi_3) + B}, \tag{3.1}$$

where B is any constant that ensures the radicand positive (in all numerical examples, we let $B = 10$). Then, we rewrite the system (2.13)–(2.16) to the following equivalent form with unknown variables $(\mathbf{u}, p, \phi_i, \mu_i, U)$:

$$\phi_{it} + (\mathbf{u} \cdot \nabla)(\phi_i - \hat{\phi}_i^0) + (\nabla \cdot \mathbf{u})(\phi_i - \hat{\phi}_i^0) = -M\frac{\bar{\mu}_i}{\Sigma_i}, \tag{3.2}$$

$$\mu_i = -\frac{3}{4}\epsilon\Sigma_i\Delta\phi_i + \frac{12}{\epsilon}(H_i + \beta)U, \quad i = 1, 2, 3, \tag{3.3}$$

$$U_t = \frac{1}{2}\sum_{i=1}^{3} H_i\phi_{it}, \tag{3.4}$$

$$\mathbf{u}_t + \mathbf{B}(\mathbf{u}, \mathbf{u}) - \nu\Delta\mathbf{u} + \nabla p - \sum_{i=1}^{3}\bar{\mu}_i\nabla(\phi_i - \hat{\phi}_i^0) + \sum_{i=1}^{3}\nabla((\phi_i - \hat{\phi}_i^0)\bar{\mu}_i) = 0, \tag{3.5}$$

$$\nabla \cdot \mathbf{u} = 0, \tag{3.6}$$

where

$$\mathbf{B}(\mathbf{u},\mathbf{v}) = (\mathbf{u}\cdot\nabla)\mathbf{v} + \frac{1}{2}(\nabla\cdot\mathbf{u})\mathbf{v}, \tag{3.7}$$

$$\hat{\phi}_i^0 = \frac{1}{|\Omega|}\int_\Omega \phi_i^0 d\mathbf{x}, \tag{3.8}$$

$$\beta = -\frac{1}{\Sigma_T}\left(\frac{H_1}{\Sigma_1} + \frac{H_2}{\Sigma_2} + \frac{H_3}{\Sigma_3}\right), \tag{3.9}$$

$$H_i = \frac{f_i}{\sqrt{F(\phi_1,\phi_2,\phi_3)+B}}. \tag{3.10}$$

The transformed system (3.2)–(3.6) in terms with the variables $(\mathbf{u},\phi_i,\mu_i,U,p)$ form a closed PDE system with the following initial conditions:

$$\begin{cases} \mathbf{u}|_{(t=0)} = \mathbf{u}^0, \quad p|_{(t=0)} = p^0, \quad \phi_i|_{(t=0)} = \phi_i^0, \quad i=1,2,3, \\ U|_{(t=0)} = U^0 = \sqrt{F(\phi_1^0,\phi_2^0,\phi_3^0)+B}. \end{cases} \tag{3.11}$$

Note the boundary conditions for U are not needed at all since Eq. (3.4) is only an ODE with time. Thus, the boundary conditions of the new system (3.2)–(3.6) are still (2.12).

We have made several modifications to the PDE model and thus we list some detailed remarks as follows.

Remark 3.1. We replace the advection term by the skew-symmetric form $\mathbf{B}(\mathbf{u},\mathbf{v})$ in the momentum equation. Even though $\nabla\cdot\mathbf{u}\neq 0$, the identity $(\mathbf{B}(\mathbf{u},\mathbf{v}),\mathbf{v}) = 0$ still holds as long as the boundary condition $\mathbf{u}\cdot\mathbf{n}|_{\partial\Omega} = 0$ is valid, which helps to preserve the discrete energy stability.

Remark 3.2. It is easy to see the convective terms in (3.2) and the stress terms in (3.5) are equivalent to that their original forms in (2.13) and (2.15) due to the divergence-free condition. These modified formulations help to ensure the perfect mixture condition (2.2) of the numerical solutions and the energy stability when developing discrete schemes. Because while using the projection methods to deal with the Navier–Stokes equations, the velocity used to discretize the convective term may not follow the divergence-free condition. Hence, the numerical solutions of ϕ_i may violate the condition (2.2) if we use the original convective term in (2.7). For comparisons, after taking the new convective terms in (2.13), by taking the summation for (2.13) for $i=1,2,3$, the convective terms turn into

$$(\mathbf{u}\cdot\nabla)\left(\sum_{i=1}^3\phi_i - \sum_{i=1}^3\hat{\phi}_i^0\right) + (\nabla\cdot\mathbf{u})\left(\sum_{i=1}^3\phi_i - \sum_{i=1}^3\hat{\phi}_i^0\right), \tag{3.12}$$

which vanishes as long as $\sum_{i=1}^3\phi_i = 1$ (since $\sum_{i=1}^3\hat{\phi}_i^0 = 1$) even if the divergence-free condition of $\mathbf{u}$ does not hold.

Using the second-order backward differentiation formula (BDF2), we now construct a time marching scheme to discretize the new system (3.2)–(3.6), that includes the following two steps:

Step 1. We compute $\tilde{\mathbf{u}}^{n+1}, \phi_i^{n+1}, \mu_i^{n+1}, U^{n+1}$ by

$$\frac{3\tilde{\mathbf{u}}^{n+1} - 4\mathbf{u}^n + \mathbf{u}^{n-1}}{2\delta t} + \mathbf{B}(\mathbf{u}^*, \tilde{\mathbf{u}}^{n+1}) - \nu\Delta\tilde{\mathbf{u}}^{n+1} + \nabla p^n$$
$$- \sum_{i=1}^{3} \bar{\mu}_i^{n+1}\nabla(\phi_i^* - \hat{\phi}_i^0) + \sum_{i=1}^{3} \nabla((\phi_i^* - \hat{\phi}_i^0)\bar{\mu}_i^{n+1}) = 0, \tag{3.13}$$

$$\frac{3\phi_i^{n+1} - 4\phi_i^n + \phi_i^{n-1}}{2\delta t} + (\tilde{\mathbf{u}}^{n+1}\cdot\nabla)(\phi_i^* - \hat{\phi}_i^0) + (\nabla\cdot\tilde{\mathbf{u}}^{n+1})(\phi_i^* - \hat{\phi}_i^0)$$
$$= -M\frac{\bar{\mu}_i^{n+1}}{\Sigma_i}, \tag{3.14}$$

$$\mu_i^{n+1} = -\frac{3}{4}\epsilon\Sigma_i\Delta\phi_i^{n+1} + \frac{12}{\epsilon}(H_i^* + \beta^*)U^{n+1} + \frac{S}{\epsilon}\Sigma_i(\phi_i^{n+1} - \phi_i^*), \quad i = 1, 2, 3, \tag{3.15}$$

$$3U^{n+1} - 4U^n + U^{n-1} = \frac{1}{2}\sum_{i=1}^{3} H_i^*(3\phi_i^{n+1} - 4\phi_i^n + \phi_i^{n-1}), \tag{3.16}$$

where

$$\begin{cases} \mathbf{u}^* = 2\mathbf{u}^n - \mathbf{u}^{n-1}, \quad \phi^* = 2\phi^n - \phi^{n-1}, \\ H^* = H(\phi_1^*, \phi_2^*, \phi_3^*), \quad \beta^* = -\dfrac{1}{\Sigma_T}\left(\dfrac{H_1^*}{\Sigma_1} + \dfrac{H_2^*}{\Sigma_2} + \dfrac{H_3^*}{\Sigma_3}\right), \end{cases} \tag{3.17}$$

S is a positive stabilization parameter, and the boundary conditions are either periodic or

$$\tilde{\mathbf{u}}^{n+1}|_{\partial\Omega} = \mathbf{0}, \quad \partial_{\boldsymbol{n}}\phi_i^{n+1}|_{\partial\Omega} = 0. \tag{3.18}$$

Step 2. We compute $p^{n+1}, \mathbf{u}^{n+1}$ as follows:

$$\frac{3}{2\delta t}(\mathbf{u}^{n+1} - \tilde{\mathbf{u}}^{n+1}) + \nabla(p^{n+1} - p^n) = 0, \tag{3.19}$$

$$\nabla\cdot\mathbf{u}^{n+1} = 0, \tag{3.20}$$

where the boundary condition is either periodic or

$$\mathbf{u}^{n+1}\cdot\boldsymbol{n}|_{\partial\Omega} = 0. \tag{3.21}$$

Remarkably, we add an extra linear, second-order stabilization term associated with S in (3.15). This term introduces an error in the scale of $S(\delta t)^2\partial_{tt}\phi_i(\cdot)$ which is comparable with the error introduced by the second-order extrapolation of the nonlinear term (see also in Refs. 5,27,29–32). In Sec. 4, we present enough numerical evidence to show that this stabilizer is critical to maintain the accuracy and improve

the energy stability while using large time steps, see the accuracy/stability tests shown in Figs. 1 and 2.

Remark 3.3. The computations of the second-order scheme (3.13)–(3.21) need the values of ϕ_i^1, U^1, p^1, $\mathbf{u}^1$. In practice, we obtain these values by constructing a first-order scheme based on the backward Euler method that reads as the following.

Step 1. We compute $\tilde{\mathbf{u}}^1, \phi_i^1, \mu_i^1, U^1$ by

$$\frac{\tilde{\mathbf{u}}^1 - \mathbf{u}^0}{2\delta t} + \mathbf{B}(\mathbf{u}^0, \tilde{\mathbf{u}}^1) - \nu\Delta\tilde{\mathbf{u}}^1 + \nabla p^0 - \sum_{i=1}^{3} \bar{\mu}_i^1 \nabla(\phi_i^0 - \hat{\phi}_i^0) + \sum_{i=1}^{3} \nabla((\phi_i^0 - \hat{\phi}_i^0)\bar{\mu}_i^1) = 0, \tag{3.22}$$

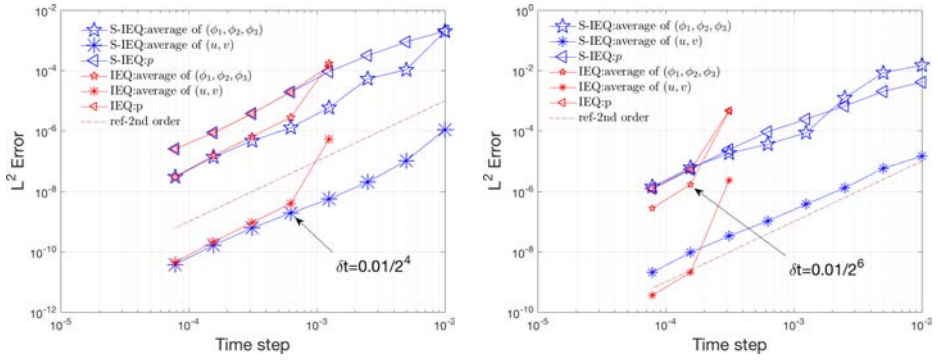

(a) S-IEQ/IEQ, $(\sigma_{12}, \sigma_{13}, \sigma_{23}) = 0.01(1, 1, 1)$. (b) S-IEQ/IEQ, $(\sigma_{12}, \sigma_{13}, \sigma_{23}) = 0.01(1, 1, 3)$.

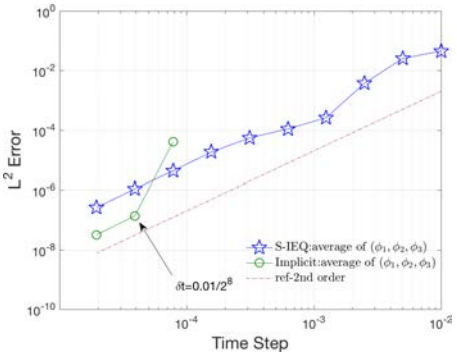

(c) S-IEQ/Implicit, $(\sigma_{12}, \sigma_{13}, \sigma_{23}) = 0.01(1, 1, 3)$.

Fig. 1. The L^2 numerical errors of unknown variables computed by using the schemes S-IEQ, IEQ, and implicit with various temporal resolutions, where (a) S-IEQ and IEQ for all unknown variables with surface tension parameters $(\sigma_{12}, \sigma_{13}, \sigma_{23}) = 0.01(1, 1, 1)$, (b) S-IEQ and IEQ with $(\sigma_{12}, \sigma_{13}, \sigma_{23}) = 0.01(1, 1, 3)$, and (c) S-IEQ and implicit with $(\sigma_{12}, \sigma_{13}, \sigma_{23}) = 0.01(1, 1, 3)$.

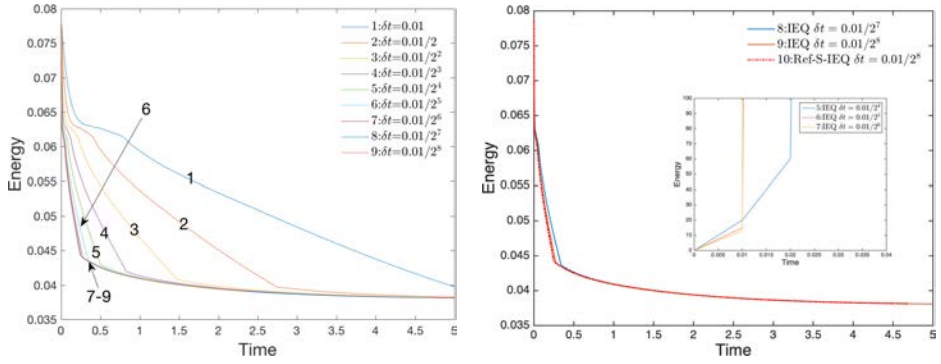

(a) S-IEQ. (b) IEQ.

Fig. 2. Time evolution of the total free energy with various time steps computed by using the scheme (a) S-IEQ and (b) IEQ with various time steps from $\delta t = 0.01$ to $\delta t = 0.01/2^8$ with a factor of $1/2$ for each variance, where the surface tension parameters are set as $(\sigma_{12}, \sigma_{13}, \sigma_{23}) = 0.01(1, 1, 3)$ (In (b), the energy evolution curves with larger time steps computed by IEQ are plotted, and it can be seen that they blow up).

$$\frac{\phi_i^1 - \phi_i^0}{\delta t} + (\tilde{\mathbf{u}}^1 \cdot \nabla)(\phi_i^0 - \hat{\phi}_i^0) + (\nabla \cdot \tilde{\mathbf{u}}^1)(\phi_i^0 - \hat{\phi}_i^0) = -M\frac{\bar{\mu}_i^1}{\Sigma_i}, \tag{3.23}$$

$$\mu_i^1 = -\frac{3}{4}\epsilon\Sigma_i\Delta\phi_i^1 + \frac{12}{\epsilon}(H_i^0 + \beta^0)U^1 + \frac{S}{\epsilon}\Sigma_i(\phi_i^1 - \phi_i^0), \quad i = 1, 2, 3, \tag{3.24}$$

$$U^1 - U^0 = \frac{1}{2}\sum_{i=1}^{3} H_i^0(\phi_i^1 - \phi_i^0). \tag{3.25}$$

Step 2. We compute $p^1, \mathbf{u}^1$ as follows:

$$\frac{1}{\delta t}(\mathbf{u}^1 - \tilde{\mathbf{u}}^1) + \nabla(p^1 - p^0) = 0, \tag{3.26}$$

$$\nabla \cdot \mathbf{u}^1 = 0. \tag{3.27}$$

The boundary condition for $\tilde{\mathbf{u}}^1, \mathbf{u}^1, \phi_i^1, \mu_i^1$ follows the same boundary conditions as the scheme (3.13)–(3.21).

The following theorem ensures the numerical solutions $(\phi_1^{n+1}, \phi_2^{n+1}, \phi_3^{n+1})$ computed by the scheme (3.13)–(3.21) always satisfy the hyperplane link condition $\sum_{i=1}^3 \phi_i^{n+1} = 1$, namely, no volume loss for the whole discrete scheme.

Theorem 3.1. *The system* (3.14)–(3.15) *is equivalent to the following scheme with two phase-field variables,*

$$\frac{3\phi_i^{n+1} - 4\phi_i^n + \phi_i^{n-1}}{2\delta t} + (\tilde{\mathbf{u}}^{n+1} \cdot \nabla)(\phi_i^* - \hat{\phi}_i^0) + (\nabla \cdot \tilde{\mathbf{u}}^{n+1})(\phi_i^* - \hat{\phi}_i^0)$$
$$= -M\frac{\bar{\mu}_i^{n+1}}{\Sigma_i}, \tag{3.28}$$

$$\mu_i^{n+1} = -\frac{3}{4}\epsilon\Sigma_i\Delta\phi_i^{n+1} + \frac{12}{\epsilon}(H_i^* + \beta^*)U^{n+1} + \frac{S}{\epsilon}\Sigma_i(\phi_i^{n+1} - \phi_i^*), \quad i = 1, 2, \tag{3.29}$$

with

$$\phi_3^{n+1} = 1 - \phi_1^{n+1} - \phi_2^{n+1}, \tag{3.30}$$

$$\frac{\mu_3^{n+1}}{\Sigma_3} = -\left(\frac{\mu_1^{n+1}}{\Sigma_1} + \frac{\mu_2^{n+1}}{\Sigma_2}\right). \tag{3.31}$$

Proof. First, assuming that (3.28)–(3.31) are satisfied, we derive (3.14)–(3.15).

From (3.31), we derive

$$\frac{\bar{\mu}_3^{n+1}}{\Sigma_3} = -\left(\frac{\bar{\mu}_1^{n+1}}{\Sigma_1} + \frac{\bar{\mu}_2^{n+1}}{\Sigma_2}\right). \tag{3.32}$$

Taking the summation of (3.28) for $i = 1, 2$, applying (3.30) at $t = t^{n+1}, t^n, t^{n-1}$, using (3.32) and $\sum_{i=1}^3 \hat{\phi}_i^0 = 1$, we obtain

$$\frac{3\phi_3^{n+1} - 4\phi_3^n + \phi_3^{n-1}}{2\delta t} + (\tilde{\mathbf{u}}^{n+1}\cdot\nabla)(\phi_3^* - \hat{\phi}_3^0) + (\nabla\cdot\tilde{\mathbf{u}}^{n+1})(\phi_3^* - \hat{\phi}_3^0) = -M\frac{\bar{\mu}_3^{n+1}}{\Sigma_3}. \tag{3.33}$$

Furthermore, from (3.31), (3.30) and the definition of β^* in (3.17), we derive

$$\begin{aligned}
\mu_3^{n+1} &= -\Sigma_3\left(\frac{\mu_1^{n+1}}{\Sigma_1} + \frac{\mu_2^{n+1}}{\Sigma_2}\right)\\
&= -\Sigma_3\left(-\frac{3}{4}\epsilon\Delta\phi_1^{n+1} - \frac{3}{4}\epsilon\Delta\phi_2^{n+1} + \frac{12}{\epsilon}\left(\frac{H_1^* + \beta^*}{\Sigma_1} + \frac{H_2^* + \beta^*}{\Sigma_2}\right)U^{n+1}\right.\\
&\quad \left. + \frac{S}{\epsilon}(\phi_1^{n+1} + \phi_2^{n+1} - \phi_1^* + \phi_2^*)\right)\\
&= -\frac{3}{4}\epsilon\Sigma_3\Delta\phi_3^{n+1} + \frac{12}{\epsilon}(H_3^* + \beta^*)U^{n+1} + \frac{S}{\epsilon}\Sigma_3(\phi_3^{n+1} - \phi_3^*).
\end{aligned}$$

Second, we then assume that Eqs. (3.14)–(3.15) are satisfied and derive (3.28)–(3.31). We use the math induction and assume (3.30) are valid for $t = t^n$ and $t = t^{n-1}$ (the validity of (3.30) at $t = t^1$ can be shown by taking the similar procedure of proof for the first-order scheme (3.22)–(3.27)). For any m, we define

$$\Phi^m = \phi_1^m + \phi_2^m + \phi_3^m, \quad \mu^m = \frac{\mu_1^m}{\Sigma_1} + \frac{\mu_2^m}{\Sigma_2} + \frac{\mu_3^m}{\Sigma_3}. \tag{3.34}$$

By taking the summation of (3.14) for $i = 1, 2, 3$, we derive

$$\frac{3}{2\delta t}(\Phi^{n+1} - 1) = -M\bar{\mu}^{n+1}, \tag{3.35}$$

where the combination of three convective terms vanishes since

$$(\tilde{\mathbf{u}}^{n+1}\cdot\nabla)\left(\sum_{i=1}^{3}\phi_i^*-\sum_{i=1}^{3}\hat{\phi}_i^0\right)+(\nabla\cdot\tilde{\mathbf{u}}^{n+1})\left(\sum_{i=1}^{3}\phi_i^*-\sum_{i=1}^{3}\hat{\phi}_i^0\right)=0, \tag{3.36}$$

where we use $\sum_{i=1}^{3}\phi_i^*=1$ by the induction.

By taking the summation of (3.15) for $i=1,2,3$, we derive

$$\mu^{n+1}=-\frac{3}{4}\epsilon\Delta\Phi^{n+1}+\frac{S}{\epsilon}(\Phi^{n+1}-1). \tag{3.37}$$

By taking the L^2 inner product of (3.35) with $-\frac{2\delta t}{3}\bar{\mu}^{n+1}$, of (3.37) with $\Phi^{n+1}-1$, and taking the summation of the two obtained equalities, we derive

$$\frac{3}{4}\epsilon\|\nabla\Phi^{n+1}\|^2+\frac{S}{\epsilon}\|\Phi^{n+1}-1\|^2+\frac{2\delta t}{3}M\|\bar{\mu}^{n+1}\|^2=0, \tag{3.38}$$

where we use $\int_\Omega(\Phi^{n+1}-1)d\mathbf{x}=\int_\Omega\bar{\mu}^{n+1}d\mathbf{x}=0$. Since the left-hand side of (3.38) is a sum of non-negative terms, thus $\bar{\mu}^{n+1}=0$ that implies $\Phi^{n+1}=1$, i.e. (3.30) is valid. Hence, from (3.37), we get $\mu^{n+1}=0$ that implies (3.31). □

The practical implementation process is described here. In fact, the new variable U^{n+1} is not needed to be solved together with ϕ_i^{n+1}. We rewrite (3.16) as

$$U^{n+1}=\frac{1}{2}\sum_{i=1}^{3}H_i^*\phi_i^{n+1}+g^n, \tag{3.39}$$

where

$$g^n=\frac{4U^n-U^{n-1}}{3}-\frac{1}{2}\sum_{i=1}^{3}H_i^*\frac{4\phi_i^n-\phi_i^{n-1}}{3}. \tag{3.40}$$

Thus, the system (3.13)–(3.16) can be rewritten as

$$\begin{aligned}&\tilde{\mathbf{u}}^{n+1}+\frac{2\delta t}{3}\mathbf{B}(\mathbf{u}^*,\tilde{\mathbf{u}}^{n+1})-\frac{2\delta t}{3}\nu\Delta\tilde{\mathbf{u}}^{n+1},\\&\quad-\frac{2\delta t}{3}\sum_{i=1}^{3}\bar{\mu}_i^{n+1}\nabla(\phi_i^*-\hat{\phi}_i^0)+\frac{2\delta t}{3}\sum_{i=1}^{3}\nabla((\phi_i^*-\hat{\phi}_i^0)\bar{\mu}_i^{n+1})=\boldsymbol{g}_1,\end{aligned} \tag{3.41}$$

$$\phi_i^{n+1}+\frac{2\delta t}{3}(\tilde{\mathbf{u}}^{n+1}\cdot\nabla)(\phi_i^*-\hat{\phi}_i^0)+\frac{2\delta t}{3}(\nabla\cdot\tilde{\mathbf{u}}^{n+1})(\phi_i^*-\hat{\phi}_i^0)+\frac{2\delta t}{3}\frac{\bar{\mu}_i^{n+1}}{\Sigma_i}=g_2^i, \tag{3.42}$$

$$-\mu_i^{n+1}-\frac{3}{4}\epsilon\Sigma_i\Delta\phi_i^{n+1}+\frac{6}{\epsilon}(H_i^*+\beta^*)\sum_{i=1}^{3}H_i^*\phi_i^{n+1}+\frac{S}{\epsilon}\Sigma_i\phi_i^{n+1}=g_3^i, \tag{3.43}$$

where $\boldsymbol{g}_1,g_2^i,g_3^i$ include all explicit terms in each corresponding equation. Note the new auxiliary variable U^{n+1} disappears in the above scheme, hence we solve the system (3.41)–(3.43) first and update U^{n+1} by (3.39).

We develop the associated weak form of the system (3.41)–(3.43) and show its well-posedness. For simplicity, the periodic boundary conditions are only considered in this paper. For the physical boundary conditions (3.18)–(3.21), the proof can be derived similarly without any essential difficulties. We define three Sobolev spaces as follows:

$$H^k_{\rm per}(\Omega) = \{\phi \in H^k(\Omega) : \phi \text{ is periodic}\},$$
$$\bar{H}^k(\Omega) = \left\{\phi \in H^k_{\rm per}(\Omega) : \int_\Omega \phi d\mathbf{x} = 0\right\},$$
$$H^k_{\mathbf{u}}(\Omega) = \{\mathbf{u} \in [H^k_{\rm per}(\Omega)]^d\},$$

where Ω is the computed domain that is a smooth, open bounded, connected domain in R^d, $d = 2, 3$.

By integrating (3.42), we obtain

$$\int_\Omega \phi_i^{n+1} d\mathbf{x} = \int_\Omega \phi_i^n d\mathbf{x} = \cdots = \int_\Omega \phi_i^0 d\mathbf{x}, \tag{3.44}$$

for $i = 1, 2, 3$. We let

$$\mathbf{u} = \tilde{\mathbf{u}}^{n+1}, \quad \phi_i = \phi_i^{n+1} - \frac{1}{|\Omega|}\int_\Omega \phi_i^0 d\mathbf{x}, \quad \mu_i = \bar{\mu}_i^{n+1}. \tag{3.45}$$

Hence, we derive $\sum_{i=1}^3 \phi_i = 0$ from Theorem 3.1.

The weak form of (3.41)–(3.43) can be formulated as follows. Find $\phi_i \in \bar{H}^1(\Omega)$, $\mu_i \in \bar{H}^0(\Omega)$, $\mathbf{u} \in H^1_{\mathbf{u}}(\Omega)$ via

$$\begin{aligned}
&(\mathbf{u}, \mathbf{v}) + \frac{2\delta t}{3}(\mathbf{B}(\mathbf{u}^*, \mathbf{u}), \mathbf{v}) + \frac{2\delta t}{3}\nu(\nabla \mathbf{u}, \nabla \mathbf{v}) \\
&\quad - \frac{2\delta t}{3}\left(\sum_{i=1}^3 \mu_i \nabla(\phi_i^* - \hat{\phi}_i^0), \mathbf{v}\right) - \frac{2\delta t}{3}\sum_{i=1}^3((\phi_i^* - \hat{\phi}_i^0)\mu_i, \nabla \cdot \mathbf{v}) \\
&\quad = (\tilde{\boldsymbol{g}}_{\mathbf{1}}, \mathbf{v}),
\end{aligned} \tag{3.46}$$

$$\begin{aligned}
&(\phi_i, w_i) + \frac{2\delta t}{3}((\mathbf{u} \cdot \nabla)(\phi_i^* - \hat{\phi}_i^0), w_i) + \frac{2\delta t}{3}((\nabla \cdot \mathbf{u})(\phi_i^* - \hat{\phi}_i^0), w_i) \\
&\quad + \frac{2\delta t}{3}\frac{M}{\Sigma_i}(\mu_i, w_i) = (\tilde{g}_2^i, w_i),
\end{aligned} \tag{3.47}$$

$$\begin{aligned}
&-(\mu_i, \psi_i) + \frac{3}{4}\epsilon\Sigma_i(\nabla\phi_i, \nabla\psi_i) + \frac{6}{\epsilon}(H_i^* + \beta^*)\left(\sum_{i=1}^3 H_i^*\phi_i, \psi_i\right) \\
&\quad + \frac{S}{\epsilon}\Sigma_i(\phi_i, \psi_i) = (\tilde{g}_3^i, \psi_i),
\end{aligned} \tag{3.48}$$

for any $\psi_i \in \bar{H}^1(\Omega)$, $w_i \in \bar{H}^0(\Omega)$, $\mathbf{v} \in H^1_{\mathbf{u}}(\Omega)$, where $\tilde{\boldsymbol{g}}_{\mathbf{1}}, \tilde{g}_2^i, \tilde{g}_3^i$ include corresponding explicit terms in each equation.

We denote the above linear system (3.46)–(3.48) as

$$(\mathbb{L}(\boldsymbol{X}), \boldsymbol{Y}) = (\mathbb{B}, \boldsymbol{Y}), \tag{3.49}$$

where $\boldsymbol{X} = (\mathbf{u},\ \mu_i,\ \phi_i)^T$, $\boldsymbol{Y} = (\mathbf{v},\ w_i,\ \psi_i)^T$, $\boldsymbol{X},\ \boldsymbol{Y} \in (H^1_{\mathbf{u}},\ \bar{H}^0,\ \bar{H}^1)(\Omega)$, and $\mathbb{B} = (\tilde{\boldsymbol{g}}_{\mathbf{1}}, \tilde{g}^i_2, \tilde{g}^i_3)^T$.

Next, we will show the well-posedness of the linear system (3.49).

Theorem 3.2. *There exists a unique solution* $(\mathbf{u}, \mu_i, \phi_i) \in (H^1_{\mathbf{u}},\ \bar{H}^0,\ \bar{H}^1)(\Omega)$ *for the linear system* (3.49).

Proof. (i). By setting $\boldsymbol{X} = (\mathbf{u},\ \mu_i,\ \phi_i)^T$ and $\boldsymbol{Y} = (\mathbf{v},\ w_i,\ \psi_i)^T$ where $\boldsymbol{X}, \boldsymbol{Y} \in (H^1_{\mathbf{u}},\ \bar{H}^0,\ \bar{H}^1)(\Omega)$, we obtain

$$\begin{aligned}(\mathbb{L}(\boldsymbol{X}), \boldsymbol{Y}) \le C_1 &\left(\|\mathbf{u}\|_{H^1} + \sum_{i=1}^{3} \|\mu_i\|_{H^0} + \sum_{i=1}^{3} \|\phi_i\|_{H^1} \right) \\ &\times \left(\|\mathbf{v}\|_{H^1} + \sum_{i=1}^{3} \|w_i\|_{H^0} + \sum_{i=1}^{3} \|\psi_i\|_{H^1} \right),\end{aligned}$$

where C_1 is some constant that may depend on $\delta t, M, \nu, \Sigma_i, S, \epsilon$, $\|\nabla \mathbf{u}^*\|_{L^\infty}$, $\|\mathbf{u}^*\|_{L^\infty}$, $\|\phi_i^*\|_{L^\infty}$, $\|\phi_i^0\|_{L^\infty}$,$\|\nabla \phi_i^*\|_{L^\infty}$, $\|\nabla \phi_i^0\|_{L^\infty}$, $\|\beta^*\|_{L^\infty}$, and $\|H^*\|_{L^\infty}$.

(ii). It is easy to find that

$$\begin{aligned}(\mathbb{L}(\boldsymbol{X}), \boldsymbol{X}) &= \|\mathbf{u}\|^2 + \frac{2\delta t}{3}\nu \|\nabla \mathbf{u}\|^2 \\ &\quad + \sum_{i=1}^{3} \left(\frac{2\delta t}{3} M \Sigma_i \left\| \frac{\mu_i}{\Sigma_i} \right\|^2 + \frac{3}{4}\epsilon \Sigma_i \|\nabla \phi_i\|^2 + \frac{S}{\epsilon} \Sigma_i \|\phi_i\|^2 \right) \\ &\quad + \frac{6}{\epsilon} \|H_1^* \phi_1 + H_2^* \phi_2 + H_3^* \phi_3\|^2 \\ &\ge \|\mathbf{u}\|^2 + \frac{2\delta t}{3}\nu \|\nabla \mathbf{u}\|^2 \\ &\quad + \sum_{i=1}^{3} \left(\frac{2\delta t}{3} M \underline{\Sigma} \left\| \frac{\mu_i}{\Sigma_i} \right\|^2 + \frac{3}{4}\epsilon \underline{\Sigma} \|\nabla \phi_i\|^2 + \frac{S}{\epsilon} \underline{\Sigma} \|\phi_i\|^2 \right) \\ &\quad + \frac{6}{\epsilon} \|H_1^* \phi_1 + H_2^* \phi_2 + H_3^* \phi_3\|^2 \\ &\ge C_2 \left(\|\mathbf{u}\|^2_{H^1} + \sum_{i=1}^{3} (\|\phi_i\|^2_{H^1} + \|\mu_i\|^2_{H^0}) \right),\end{aligned}$$

where we use Lemma 2.1 since $\sum_{i=1}^{3} \frac{\mu_i}{\Sigma_i} = 0$ from (3.31) and $\sum_{i=1}^{3} \phi_i = 0$. The constant C_2 depends on $\delta t, M, \underline{\Sigma}, \nu, S, \epsilon$.

Therefore, we conclude that the linear system (3.49) admits a unique solution $\boldsymbol{X} = (\mathbf{u}, \mu_i, \phi_i)^T \in (H^1_{\mathbf{u}},\ \bar{H}^0,\ \bar{H}^1)(\Omega)$ by using the Lax–Milgram theorem. □

The unconditional energy stability of the scheme (3.13)–(3.21) is shown as follows.

Theorem 3.3. *The time-discrete scheme* (3.13)–(3.21) *satisfies the discrete energy dissipation law as follows*:

$$\frac{1}{\delta t}(E^{n+1}-E^n) \le -\nu\|\nabla\tilde{\mathbf{u}}^{n+1}\|^2 - M\underline{\Sigma}\sum_{i=1}^{3}\left\|\frac{\bar{\mu}_i^{n+1}}{\Sigma_i}\right\|^2 \le 0, \tag{3.50}$$

where $E^{n+1} \ge 0$ *is defined as*

$$\begin{aligned} E^{n+1} = {} & \frac{1}{2}\left(\frac{1}{2}\|\mathbf{u}^{n+1}\|^2 + \frac{1}{2}\|2\mathbf{u}^{n+1}-\mathbf{u}^n\|^2\right) + \frac{(\delta t)^2}{3}\|\nabla p^{n+1}\|^2 \\ & + \frac{3\epsilon}{8}\sum_{i=1}^{3}\left(\Sigma_i\left(\frac{1}{2}\|\nabla\phi_i^{n+1}\|^2 + \frac{1}{2}\|2\nabla\phi_i^{n+1}-\nabla\phi_i^n\|^2\right)\right) \\ & + \frac{12}{\epsilon}\left(\frac{1}{2}\|U^{n+1}\|^2 + \frac{1}{2}\|2U^{n+1}-U^n\|^2\right) \\ & + \frac{S}{2\epsilon}\sum_{i=1}^{3}(\Sigma_i\|\phi_i^{n+1}-\phi_i^n\|^2). \end{aligned} \tag{3.51}$$

Proof. It is easy to see that $E^{n+1} \ge 0$ by using Lemma 2.1 and (3.30).

By taking the inner product of (3.13) with $2\delta t\tilde{\mathbf{u}}^{n+1}$ in the L^2 space, we obtain

$$\begin{aligned} & (3\tilde{\mathbf{u}}^{n+1}-4\mathbf{u}^n+\mathbf{u}^{n-1},\tilde{\mathbf{u}}^{n+1}) + 2\nu\delta t\|\nabla\tilde{\mathbf{u}}^{n+1}\|^2 + 2\delta t(\nabla p^n,\tilde{\mathbf{u}}^{n+1}) \\ & - 2\delta t\sum_{i=1}^{3}(\bar{\mu}_i^{n+1}\nabla(\phi_i^*-\hat{\phi}_i^0),\tilde{\mathbf{u}}^{n+1}) \\ & - 2\delta t\sum_{i=1}^{3}(\phi_i^*-\hat{\phi}_i^0)\bar{\mu}_i^{n+1},\nabla\cdot\tilde{\mathbf{u}}^{n+1}) = 0. \end{aligned} \tag{3.52}$$

From (3.19), for any variable $\mathbf{v}$ with $\nabla\cdot\mathbf{v}=0$, we have

$$(\mathbf{u}^{n+1},\mathbf{v}) = (\tilde{\mathbf{u}}^{n+1},\mathbf{v}). \tag{3.53}$$

We derive following equality

$$\begin{aligned} & (3\tilde{\mathbf{u}}^{n+1}-4\mathbf{u}^n+\mathbf{u}^{n-1},\tilde{\mathbf{u}}^{n+1}) \\ & = (3\tilde{\mathbf{u}}^{n+1}-4\mathbf{u}^n+\mathbf{u}^{n-1},\mathbf{u}^{n+1}) + (3\tilde{\mathbf{u}}^{n+1}-4\mathbf{u}^n+\mathbf{u}^{n-1},\tilde{\mathbf{u}}^{n+1}-\mathbf{u}^{n+1}) \\ & = (3\mathbf{u}^{n+1}-4\mathbf{u}^n+\mathbf{u}^{n-1},\mathbf{u}^{n+1}) + (3\tilde{\mathbf{u}}^{n+1},\ \tilde{\mathbf{u}}^{n+1}-\mathbf{u}^{n+1}) \\ & = (3\mathbf{u}^{n+1}-4\mathbf{u}^n+\mathbf{u}^{n-1},\mathbf{u}^{n+1}) + 3(\tilde{\mathbf{u}}^{n+1}-\mathbf{u}^{n+1},\tilde{\mathbf{u}}^{n+1}+\mathbf{u}^{n+1}) \end{aligned}$$

$$= \frac{1}{2}(\|\mathbf{u}^{n+1}\|^2 - \|\mathbf{u}^n\|^2 + \|2\mathbf{u}^{n+1} - \mathbf{u}^n\|^2 - \|2\mathbf{u}^n - \mathbf{u}^{n-1}\|^2 + \|\mathbf{u}^{n+1} - 2\mathbf{u}^n + \mathbf{u}^{n-1}\|^2\Big) + 3(\|\tilde{\mathbf{u}}^{n+1}\|^2 - \|\mathbf{u}^{n+1}\|^2), \tag{3.54}$$

where we use the following identity

$$2(3a - 4b + c, a) = \|a\|^2 - \|b\|^2 + \|2a - b\|^2 - \|2b - c\|^2 + \|a - 2b + c\|^2. \tag{3.55}$$

We reformulate the projection step (3.19) as

$$\frac{3}{2\delta t}\mathbf{u}^{n+1} + \nabla p^{n+1} = \frac{3}{2\delta t}\tilde{\mathbf{u}}^{n+1} + \nabla p^n. \tag{3.56}$$

By taking the square of both sides of the above equation, we get

$$\frac{9}{4(\delta t)^2}\|\mathbf{u}^{n+1}\|^2 + \|\nabla p^{n+1}\|^2 = \frac{9}{4(\delta t)^2}\|\tilde{\mathbf{u}}^{n+1}\|^2 + \|\nabla p^n\|^2 + \frac{3}{\delta t}(\tilde{\mathbf{u}}^{n+1}, \nabla p^n). \tag{3.57}$$

Hence, by multiplying $2(\delta t)^2/3$ of the above equation, we derive

$$\frac{3}{2}(\|\mathbf{u}^{n+1}\|^2 - \|\tilde{\mathbf{u}}^{n+1}\|^2) + \frac{2(\delta t)^2}{3}(\|\nabla p^{n+1}\|^2 - \|\nabla p^n\|^2) = 2\delta t(\tilde{\mathbf{u}}^{n+1}, \nabla p^n). \tag{3.58}$$

By taking the inner product of (3.19) with $2\delta t\mathbf{u}^{n+1}$ in the L^2 space, we have

$$\frac{3}{2}(\|\mathbf{u}^{n+1}\|^2 - \|\tilde{\mathbf{u}}^{n+1}\|^2 + \|\mathbf{u}^{n+1} - \tilde{\mathbf{u}}^{n+1}\|^2) = 0. \tag{3.59}$$

We combine (3.52), (3.54), (3.58), and (3.59) to obtain

$$\begin{aligned}&\frac{1}{2}(\|\mathbf{u}^{n+1}\|^2 - \|\mathbf{u}^n\|^2 + \|2\mathbf{u}^{n+1} - \mathbf{u}^n\|^2 - \|2\mathbf{u}^n - \mathbf{u}^{n-1}\|^2 \\ &\quad + \|\mathbf{u}^{n+1} - 2\mathbf{u}^n + \mathbf{u}^{n-1}\|^2) + \frac{3}{2}\|\mathbf{u}^{n+1} - \tilde{\mathbf{u}}^{n+1}\|^2 \\ &\quad + \frac{2(\delta t)^2}{3}(\|\nabla p^{n+1}\|^2 - \|\nabla p^n\|^2) + 2\nu\delta t\|\nabla\tilde{\mathbf{u}}^{n+1}\|^2 \\ &\quad - 2\delta t\sum_{i=1}^{3}(\bar{\mu}_i^{n+1}\nabla(\phi_i^* - \hat{\phi}_i^0), \tilde{\mathbf{u}}^{n+1}) - 2\delta t\sum_{i=1}^{3}((\phi_i^* - \hat{\phi}_i^0)\bar{\mu}_i^{n+1}, \nabla\cdot\tilde{\mathbf{u}}^{n+1}) = 0.\end{aligned} \tag{3.60}$$

Computing the inner product of (3.14) with $2\delta t\bar{\mu}_i^{n+1}$ in the L^2 space, we have

$$\begin{aligned}&(3\phi_i^{n+1} - 4\phi_i^n + \phi_i^{n-1}, \bar{\mu}_i^{n+1}) + 2\delta t((\tilde{\mathbf{u}}^{n+1}\cdot\nabla)(\phi_i^* - \hat{\phi}_i^0), \bar{\mu}_i^{n+1}) \\ &\quad + 2\delta t((\nabla\cdot\tilde{\mathbf{u}}^{n+1})(\phi_i^* - \hat{\phi}_i^0), \bar{\mu}_i^{n+1}) + 2\delta t M\Sigma_i\left\|\frac{\bar{\mu}_i^{n+1}}{\Sigma_i}\right\|^2 = 0.\end{aligned} \tag{3.61}$$

Computing the L^2 inner product of (3.15) with $-(3\phi_i^{n+1} - 4\phi_i^n + \phi_i^{n-1})$ and applying integration by parts, we find

$$\begin{aligned}
&-(\mu_i^{n+1}, 3\phi_i^{n+1} - 4\phi_i^n + \phi_i^{n-1}) \\
&\quad = -\frac{3}{4}\epsilon\Sigma_i(\nabla\phi_i^{n+1}, \nabla(3\phi_i^{n+1} - 4\phi_i^n + \phi_i^{n-1})) \\
&\qquad - \frac{12}{\epsilon}(H_i^* U^{n+1}, 3\phi_i^{n+1} - 4\phi_i^n + \phi_i^{n-1}) \\
&\qquad - \frac{S}{\epsilon}(\Sigma_i(\phi_i^{n+1} - \phi_i^*), 3\phi_i^{n+1} - 4\phi_i^n + \phi_i^{n-1}),
\end{aligned} \tag{3.62}$$

where we use the following equality

$$\begin{aligned}
\sum_{i=1}^{3}(\beta^* U^{n+1}, 3\phi_i^{n+1} - 4\phi_i^n + \phi_i^{n-1}) &= \left(\beta^* U^{n+1}, \sum_{i=1}^{3}(3\phi_i^{n+1} - 4\phi_i^n + \phi_i^{n-1})\right) \\
&= 0,
\end{aligned} \tag{3.63}$$

which is due to (3.30). Moreover, from (3.44), it is easy to derive

$$(3\phi_i^{n+1} - 4\phi_i^n + \phi_i^{n-1}, \bar{\mu}_i^{n+1}) = (3\phi_i^{n+1} - 4\phi_i^n + \phi_i^{n-1}, \mu_i^{n+1}). \tag{3.64}$$

We compute the inner product of (3.16) with $\frac{24}{\epsilon}U^{n+1}$ in the L^2 space and use (3.55) to obtain

$$\begin{aligned}
&\frac{12}{\epsilon}(\|U^{n+1}\|^2 - \|U^n\|^2 + \|2U^{n+1} - U^n\|^2 - \|2U^n - U^{n-1}\|^2 \\
&\quad + \|U^{n+1} - 2U^n + U^{n-1}\|^2) = \frac{12}{\epsilon}\sum_{i=1}^{3}(H_i^*(3\phi_i^{n+1} - 4\phi_i^n + \phi_i^{n-1}), U^{n+1}).
\end{aligned} \tag{3.65}$$

Hence, by taking the summation for $i = 1, 2, 3$ of (3.60)–(3.62), and combining the obtained result with (3.65), we arrive at

$$\begin{aligned}
&\frac{1}{2}(\|\mathbf{u}^{n+1}\|^2 - \|\mathbf{u}^n\|^2 + \|2\mathbf{u}^{n+1} - \mathbf{u}^n\|^2 - \|2\mathbf{u}^n - \mathbf{u}^{n-1}\|^2) \\
&\quad + \frac{2(\delta t)^2}{3}(\|\nabla p^{n+1}\|^2 - \|\nabla p^n\|^2) \\
&\quad + \frac{3\epsilon}{8}\sum_{i=1}^{3}\Sigma_i(\|\nabla\phi_i^{n+1}\|^2 - \|\nabla\phi_i^n\|^2 + \|\nabla(2\phi_i^{n+1} - \phi_i^n)\|^2 - \|\nabla(2\phi_i^n - \phi_i^{n-1})\|^2) \\
&\quad + \frac{12}{\epsilon}(\|U^{n+1}\|^2 - \|U^n\|^2 + \|2U^{n+1} - U^n\|^2 - \|2U^n - U^{n-1}\|^2) \\
&\quad + \frac{S}{\epsilon}\sum_{i=1}^{3}\Sigma_i(\|\phi_i^{n+1} - \phi_i^n\|^2 - \|\phi_i^n - \phi_i^{n-1}\|^2)
\end{aligned}$$

$$
\begin{aligned}
&+\left\{\frac{1}{2}\|\mathbf{u}^{n+1}-2\mathbf{u}^{n}+\mathbf{u}^{n-1}\|^2+\frac{3}{2}\|\mathbf{u}^{n+1}-\tilde{\mathbf{u}}^{n+1}\|^2\right.\\
&+\frac{3\epsilon}{8}\sum_{i=1}^{3}\Sigma_i\|\nabla(\phi_i^{n+1}-2\phi_i^{n}+\phi_i^{n-1})\|^2\\
&+\frac{12}{\epsilon}\|U^{n+1}-2U^{n}+U^{n-1}\|^2\\
&\left.+\frac{2S}{\epsilon}\sum_{i=1}^{3}\Sigma_i\|\phi_i^{n+1}-2\phi_i^{n}+\phi_i^{n-1}\|^2\right\}\\
&=-2\delta t\nu\|\nabla\tilde{\mathbf{u}}^{n+1}\|^2-2\delta tM\sum_{i=1}^{3}\Sigma_i\left\|\frac{\bar{\mu}_i^{n+1}}{\Sigma_i}\right\|^2\\
&\le-2\delta t\nu\|\nabla\tilde{\mathbf{u}}^{n+1}\|^2-2\delta tM\underline{\Sigma}\sum_{i=1}^{3}\left\|\frac{\bar{\mu}_i^{n+1}}{\Sigma_i}\right\|^2\le 0,
\end{aligned}
\tag{3.66}
$$

where we use Lemma 2.1, (3.32), (3.64), and the following identity

$$
(3a-4b+c,a-2b+c)=\|a-b\|^2-\|b-c\|^2+2\|a-2b+c\|^2. \tag{3.67}
$$

Finally, we obtain (3.50) after dropping the terms in { } of (3.66) since they are all positive from Lemma 2.1 and (3.30), i.e.

$$
\begin{aligned}
&\sum_{i=1}^{3}\Sigma_i\|\nabla(\phi_i^{n+1}-2\phi_i^{n}+\phi_i^{n-1})\|^2\ge\underline{\Sigma}\sum_{i=1}^{3}\|\nabla(\phi_i^{n+1}-2\phi_i^{n}+\phi_i^{n-1})\|^2\ge 0,\\
&\sum_{i=1}^{3}\Sigma_i\|\phi_i^{n+1}-2\phi_i^{n}+\phi_i^{n-1}\|^2\ge\underline{\Sigma}\sum_{i=1}^{3}\|\phi_i^{n+1}-2\phi_i^{n}+\phi_i^{n-1}\|^2\ge 0.
\end{aligned}
\tag{3.68}
$$

□

4. Numerical Simulation

In this section, we perform numerical simulations in two- and three-dimensional spaces to demonstrate the accuracy and energy stability of the developed scheme (3.13)–(3.21).

4.1. *Brief description of the full discretization schemes*

In all the next simulations, we set the computational region to be a two- or three-dimensional rectangular domain as $\Omega=[0,L_1]\times[0,L_2]$ or $\Omega=[0,L_1]\times[0,L_2]\times[0,L_3]$. For the direction that is assumed to follow periodic boundary conditions, we adopt the Fourier-spectral method. For the direction that is assumed to follow the boundary conditions as (3.18)–(3.21), the spatial discretizations are based on the

Legendre–Galerkin method which results in very efficient and accurate solvers for elliptic equations with constant coefficients. We adopt the inf-sup stable $P_N \times P_{N-2}$ pair for the velocity and pressure, and P_N for the phase-field variables. For solving the coupled linear variable-coefficient system in Step 1, we refer to our recent work in Refs. 5,29 and 35 where the procedure was given in details.

4.2. *Accuracy and stability test*

We first perform accuracy and stability tests for the developed scheme (3.13)–(3.21). When the scheme is equipped with a nonzero stabilizer ($S \neq 0$), we denote it by S-IEQ for short. To show how the stability is improved by the stabilization term, for comparisons, the convergence rates of the non-stabilized version are also calculated, namely, the scheme (3.13)–(3.21) without the stabilizer ($S = 0$), denoted by IEQ for short. We also compare the convergence rates by using the second-order implicit type scheme that is based on the Crank–Nicolson approach and all nonlinear terms are treated implicitly. For convenience, we denote it by Implicit.

We first set a 2D computational domain with $(x, y) \in \Omega = [0, 2] \times [0, 1]$. We assume the periodic boundary conditions for the x-axis and then discretize it by using 257 Fourier modes. The boundary conditions (3.18) and (3.21) are used for the y-axis which is then discretized by using Legendre polynomials up to the degree of 256. The initial conditions for variables $\phi_i, \mathbf{u}, p$ are set as follows:

$$\begin{cases} \phi_i^0(x,y) = \tanh\left(\dfrac{r - \sqrt{(x-x_i)^2 + (y-y_i)^2}}{\epsilon}\right), \quad i = 1, 2, \\ \phi_3^0(x,y) = 1 - \phi_1^0(x,y) - \phi_2^0(x,y), \\ \mathbf{u}^0(x,y) = \mathbf{0}, \quad p^0(x,y) = 0, \end{cases} \tag{4.1}$$

where $r = 0.25$, $x_1 = 1.27$, $x_2 = 0.73$, $y_1 = y_2 = 0.5$. We also set $\nu = 1$, $\epsilon = 0.04$, $M = \frac{1}{\epsilon}$, $B = 10$, and $S = 10$.

Since the exact solutions are not known, we choose the numerical solutions using a very tiny time step size $\delta t = 1e - 9$ computed by using the scheme S-IEQ as the benchmark solution (approximately the exact solution) for computing errors. We investigate the order of accuracy by using two different set of surface tension parameters $(\sigma_{12}, \sigma_{23}, \sigma_{13}) = 0.01(1, 1, 1)$ and $0.01(1, 1, 3)$ by varying the time step sizes.

In Fig. 1(a), we set the partial spreading surface tension parameters as $(\sigma_{12}, \sigma_{23}, \sigma_{13}) = 0.02(1, 1, 1)$. By varying the time step size δt from $1e - 2$ to $\delta t = \frac{1e-2}{2^7}$ with a factor of $1/2$ for each variance, we show the L^2-errors of all the variables. More precisely, the average of the L^2 errors of the three phase-field variables (since the accuracy performance of the three phase-field variables are almost the same, we only plot the average value of their numerical errors), the average of the L^2 errors of the velocity field, as well as the L^2 error of the pressure between the numerical solution and the exact solution at $t = 0.2$ are plotted. We

observe that the stabilized scheme S-IEQ presents the second-order convergence rate. But the non-stabilized scheme IEQ blows up while the time step is large ($\delta t \geq \frac{0.01}{2^3}$) and presents the second-order convergence rate when $\delta t \leq \frac{0.01}{2^4}$. Similarly, in Fig. 1(b) with the total spreading coefficients $(\sigma_{12}, \sigma_{23}, \sigma_{13}) = 0.01(1, 1, 3)$, we observe that the stabilized scheme S-IEQ presents almost perfect second-order accuracy all along, but the non-stabilized scheme IEQ blows up for $\delta t \geq \frac{0.01}{2^6}$ and presents the second-order convergence rate only when $\delta t \leq \frac{0.01}{2^6}$. In Fig. 1(c) with $(\sigma_{12}, \sigma_{23}, \sigma_{13}) = 0.01(1, 1, 3)$, we compare the convergence rate computed by S-IEQ and Implicit for the average of the three phase-field variables. We observe that the Implicit scheme blows up for $\delta t > \frac{0.01}{2^7}$ and can only present the second-order convergence rate when $\delta t \leq \frac{0.01}{2^8}$.

We further plot the temporal evolution curves of the total free energy (3.51) with various time steps for the second example with $(\sigma_{12}, \sigma_{23}, \sigma_{13}) = 0.01(1, 1, 3)$. The computed energy curves computed by the scheme S-IEQ and IEQ are shown in Figs. 2(a) and 2(b), respectively. We find that all energy curves computed by the scheme S-IEQ show monotonic decays, which confirms the unconditional stability of the scheme. For comparison, in Fig. 2(b), the scheme IEQ blows up for larger time steps and only show decays when $\delta t \leq \frac{0.01}{2^7}$.

Therefore, through all accuracy and stability tests computed above, we find that the stabilized scheme S-IEQ presents better accuracy and stability results in comparisons with its non-stabilized version and Implicit type schemes especially while using large time steps.

4.3. *Spinodal decomposition with various surface tension parameters*

In this example, we study how surface tension parameters drive the system to evolve from the initial homogeneous state to a three-phase state. This is the so-called phase separation (or called spinodal decomposition) dynamics. We set the initial conditions as a homogeneous ternary mixture that reads as follows:

$$\begin{cases} \mathbf{u}^0(\mathbf{x}) = \mathbf{0}, \quad p^0(\mathbf{x}) = 0, \\ \psi_i(\mathbf{x}) = 0.5 + 0.001\text{rand}(\mathbf{x}), \\ \phi_i^0(\mathbf{x}) = \dfrac{\psi_i}{\psi_1 + \psi_2 + \psi_3}, \quad i = 1, 2, 3, \end{cases} \tag{4.2}$$

where the rand($\mathbf{x}$) is the random number in $[-1, 1]$ that follows the normal distribution.

We first perform 2D simulations using the computational domain $[0, 4]^2$ and adopting the periodic boundary conditions. Space is discretized by using the Fourier-spectral methods with 257^2 Fourier modes. The model parameters read as $\delta t = 1e-3$, $\epsilon = 0.04$, $B = 10$, $S = 20$, and $M = 250$. We adjust the surface tensions $(\sigma_{12}, \sigma_{13}, \sigma_{23})$ to investigate how the three-phase equilibrium patterns are obtained.

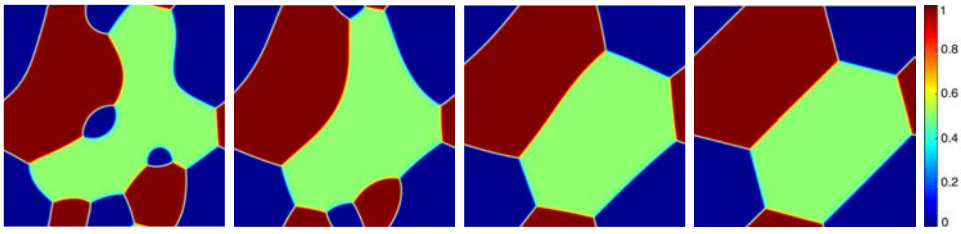

(a) $(\sigma_{12}, \sigma_{13}, \sigma_{23}) = 0.01(1, 1, 1)$.

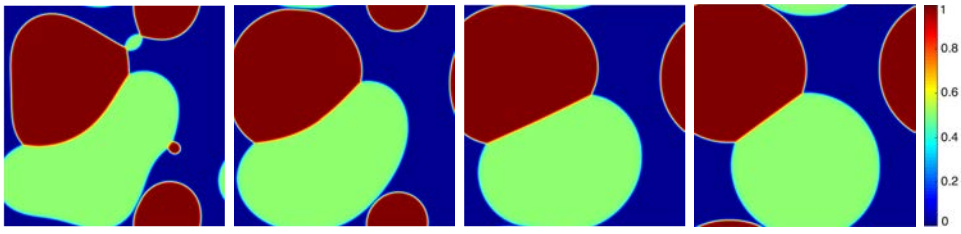

(b) $(\sigma_{12}, \sigma_{13}, \sigma_{23}) = 0.01(1, 0.6, 0.6)$.

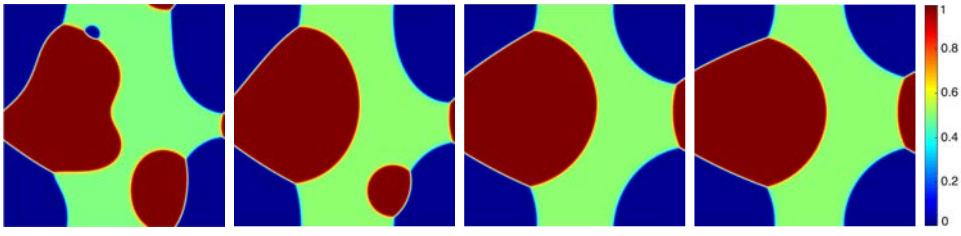

(c) $(\sigma_{12}, \sigma_{13}, \sigma_{23}) = 0.01(1, 0.8, 1.4)$.

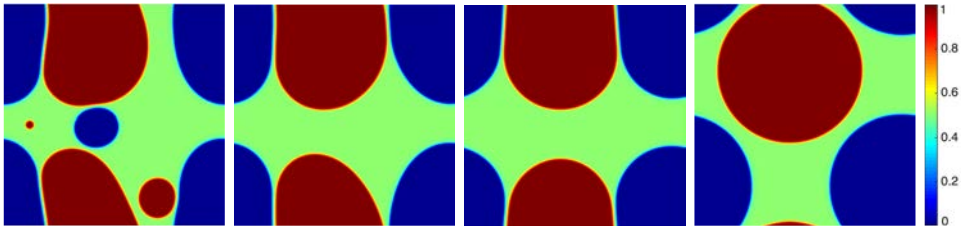

(d) $(\sigma_{12}, \sigma_{13}, \sigma_{23}) = 0.01(1, 1, 3)$.

Fig. 3. The 2D dynamical evolutions of the profile $\frac{1}{2}\phi_1 + \phi_2$ for the spinodal decomposition examples with various sets of surface tension parameters $(\sigma_{12}, \sigma_{13}, \sigma_{23})$. In each subfigure, snapshots at $t = 1$, 2, 5, and 50 (equilibrium state) are presented.

In Fig. 3, we plot the profiles of $\frac{1}{2}\phi_1 + \phi_2$ with four sets of surface tension parameters as $(\sigma_{12}, \sigma_{13}, \sigma_{23}) = 0.01(1, 1, 1)$, $0.01(1, 0.6, 0.6)$, $0.01(1, 0.8, 1.4)$, and $0.01(1, 1, 3)$. We observe that the final equilibrium solution presents various patterns with different contact angles. In particular, when $(\sigma_{12}, \sigma_{13}, \sigma_{23}) = 0.01(1, 1, 1)$,

shown in Fig. 3(a), the equilibrium solution present hexagonal phases with three equal contact angles $\frac{2\pi}{3}$ are obtained. When $(\sigma_{12}, \sigma_{13}, \sigma_{23}) = 0.01(1, 1, 3)$, shown in Fig. 3(d), no junction points are formed due to the total spreading coefficients.

We further perform 3D simulations using the computational domain $[0, 2]^3$ and adopting the periodic boundary conditions. Space is discretized by using the Fourier-spectral methods with 257^3 Fourier modes. The model parameters read as $\delta t = 1e-3$, $\epsilon = 0.04$, $B = 10$, $S = 20$, and $M = 50$. In Fig. 4, we plot 3D dynamical evolution of the isosurfaces of $\{\phi_1 = \frac{1}{2}\}$ (red) and $\{\phi_2 = \frac{1}{2}\}$ (yellow) in different colors with three surface tension parameters as $(\sigma_{12}, \sigma_{13}, \sigma_{23}) = 0.01(1, 1, 1)$, $0.01(1, 0.8, 1.4)$, and $0.01(1, 1, 3)$. We observe that the three components accumulate with different contact angles.

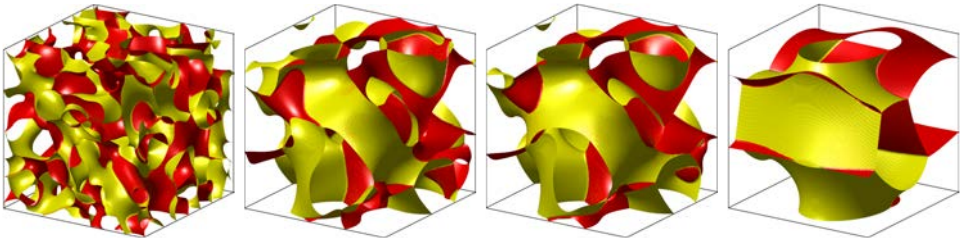

(a) $(\sigma_{12}, \sigma_{13}, \sigma_{23}) = 0.01(1, 1, 1)$, snapshots are taken at 1, 4, 5, and 20.

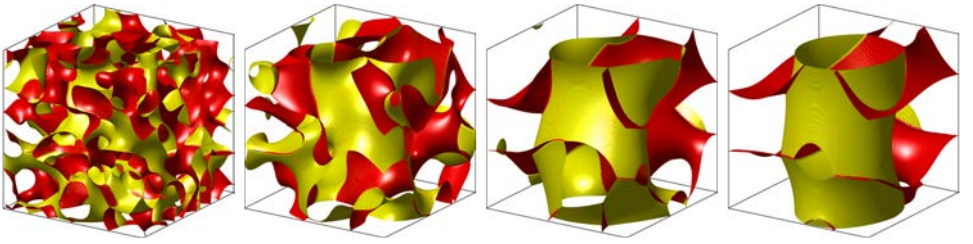

(b) $(\sigma_{12}, \sigma_{13}, \sigma_{23}) = 0.01(1, 0.8, 1.4)$, snapshots are taken at 1, 3, 7, and 20.

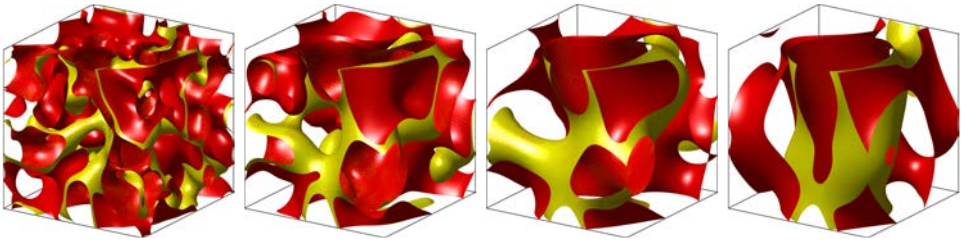

(c) $(\sigma_{12}, \sigma_{13}, \sigma_{23}) = 0.01(1, 1, 3)$, snapshots are taken at 1, 3, 7, and 20.

Fig. 4. (Color online) The 3D dynamical evolutions of the isosurfaces of $\{\phi_1 = \frac{1}{2}\}$ (red) and $\{\phi_2 = \frac{1}{2}\}$ (yellow) for the spinodal decomposition examples with various surface tension parameters are set as $(\sigma_{12}, \sigma_{13}, \sigma_{23}) = 0.01(1, 1, 1)$, $0.01(1, 0.8, 1.4)$, and $0.01(1, 1, 3)$.

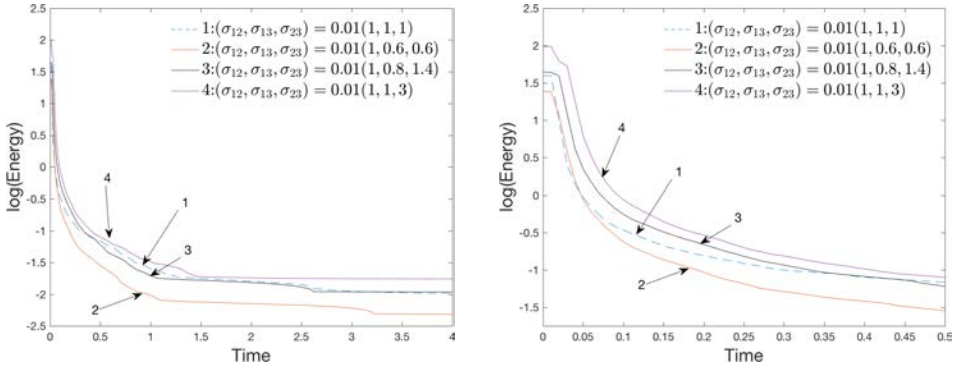

(a) Log(Energy) evolution. (b) A close-up view when the energies decay fast.

Fig. 5. Time evolution of the logarithm of the total free energy (3.51) for the 2D spinodal decomposition examples where various surface tension parameters are set as $(\sigma_{12}, \sigma_{13}, \sigma_{23}) = 0.01(1, 1, 1)$, $0.01(1, 0.6, 0.6)$, $0.01(1, 0.8, 1.4)$, and $0.01(1, 1, 3)$.

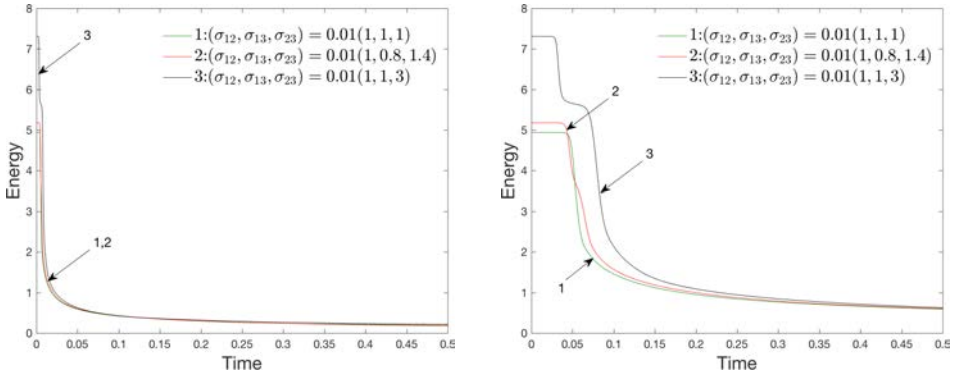

(a) Energy evolution. (b) A close-up view when the energies decay fast.

Fig. 6. Time evolution of the total free energy (3.51) for the 3D spinodal decomposition examples where various surface tension parameters are set as $(\sigma_{12}, \sigma_{13}, \sigma_{23}) = 0.01(1, 1, 1)$, $0.01(1, 0.8, 1.4)$, and $0.01(1, 1, 3)$.

In Figs. 5 and 6, we present the time evolution of the free energy functional for all 2D and 3D simulations. The energy curves show decays with the time that confirms that the developed algorithm is unconditionally stable.

4.4. *Liquid lens between two stratified fluids under the shear flow*

In this section, we investigate the evolutions of the liquid lens driven by the imposed shear flow on the boundary. We set the 2D computed domain as

$(x, y) \in \Omega = [0, 1] \times [0, 0.5]$ and the initial conditions as follows:

$$\begin{cases} \phi_1^0(x, y) = (1 - \phi_3^0)\left(\frac{1}{2} + \frac{1}{2}\tanh\left(\frac{4}{\epsilon}(y - 0.25)\right)\right), \\ \phi_2^0(x, y) = 1 - \phi_1^0 - \phi_3^0, \\ \phi_3^0(x, y) = \frac{1}{2}\tanh\left(\frac{0.09 - \sqrt{(x - 0.5)^2 + (y - 0.25)^2}}{\epsilon/2}\right) + \frac{1}{2}, \\ \mathbf{u}^0(x, y) = (0, 0), \quad p^0(x, y) = 0. \end{cases} \tag{4.3}$$

The liquid lens at the initial moment is set as circular and located at the interface between two other immiscible fluids. We set the periodic boundary conditions along the x-direction and discretize it by using the Fourier-spectral method with 257 Fourier modes. The boundary conditions for the variables along the y-direction are set as

$$u|_{(y=0,0.5)} = \pm u_w, \quad v|_{(y=0,0.5)} = \partial_{\boldsymbol{n}}\phi_i|_{(y=0,0.5)} = \partial_{\boldsymbol{n}}\mu_i|_{(y=0,0.5)} = 0, \tag{4.4}$$

where the u_w is the wall shear velocity. Hence, we discretize y-direction by using the Legendre–Galerkin spectral method with the Legendre polynomials up to the degree of 512. For better accuracy, we use the time step $\delta t = 1e - 3$. We set other model parameters as $\nu = 1, M = 100, \epsilon = 0.01, B = 10, S = 10$, and adjust the surface tension parameters $(\sigma_{12}, \sigma_{13}, \sigma_{23})$ to investigate how the contact angles are affected by the surface tension forces.

We first investigate the no shear case ($u_w = 0$) by using four partial spreading ($\Sigma_i > 0$, for all i), and two total spreading surface tension parameters ($\Sigma_i < 0$ for some i). In each subfigure of Fig. 8, we plot snapshots of the profile $\frac{1}{2}\phi_1 + \phi_2$ at various times.

From the sharp interface formula (4.5) for angles, i.e. in the limit ϵ approximates 0, the contact angles (shown in Fig. 7) at the equilibrium state of the liquid lens follow the so-called Young's relation (cf. Refs. 4,16 and 24) given as

$$\frac{\sin\theta_1}{\sigma_{23}} = \frac{\sin\theta_2}{\sigma_{13}} = \frac{\sin\theta_3}{\sigma_{12}}, \tag{4.5}$$

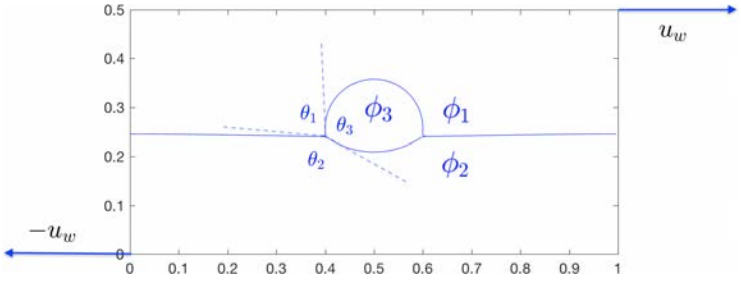

Fig. 7. Theoretical shape of the contact lens between two stratified fluid at the equilibrium state.

we derive (a) $\theta_1 = \theta_2 = \theta_3 = \frac{2\pi}{3}$ for $(\sigma_{12}, \sigma_{13}, \sigma_{23}) = 0.01(1,1,1)$; (b) $\theta_1 > \theta_2 = \theta_3$ for $(\sigma_{12}, \sigma_{13}, \sigma_{23}) = 0.01(1,1,0.6)$; (c) $\theta_1 = \theta_2 > \theta_3$ for $(\sigma_{12}, \sigma_{13}, \sigma_{23}) = 0.01(1,0.6,0.6)$; (d) $\theta_1 < \theta_3 < \theta_2$ for $(\sigma_{12}, \sigma_{13}, \sigma_{23}) = 0.01(1,0.8,1.4)$; (e) $\theta_1 = 0$, $\theta_2 = \theta_3 = \pi$ for $(\sigma_{12}, \sigma_{13}, \sigma_{23}) = 0.01(1,1,3)$; and (f) $\theta_1 = \theta_2 = \pi, \theta_3 = 0$ for

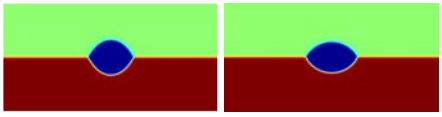

(a) $t = 0.2, 10$ with $(\sigma_{12}, \sigma_{13}, \sigma_{23}) = 0.01(1,1,1)$.

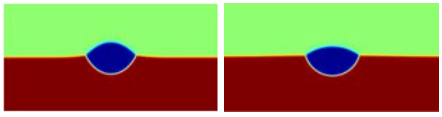

(b) $t = 0.4, 6$ with $(\sigma_{12}, \sigma_{13}, \sigma_{23}) = 0.01(1,1,0.6)$.

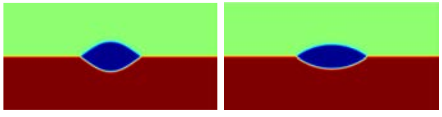

(c) $t = 0.4, 6$ with $(\sigma_{12}, \sigma_{13}, \sigma_{23}) = 0.01(1,0.6,0.6)$.

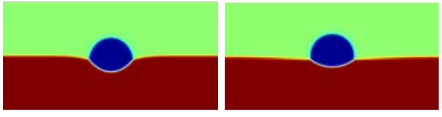

(d) $t = 0.4, 6$ with $(\sigma_{12}, \sigma_{13}, \sigma_{23}) = 0.01(1,0.8,1.4)$.

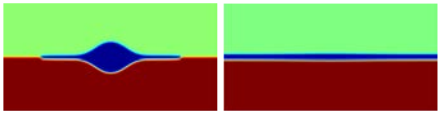

(e) $t = 0.2, 3$ with $(\sigma_{12}, \sigma_{13}, \sigma_{23}) = 0.01(3,1,1)$.

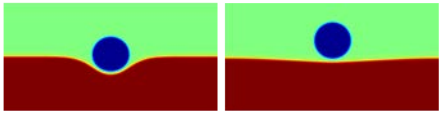

(f) $t = 0.4, 10$ with $(\sigma_{12}, \sigma_{13}, \sigma_{23}) = 0.01(1,1,3)$.

Fig. 8. The 2D dynamical evolution of the profile $\frac{1}{2}\phi_1 + \phi_2$ for the liquid lens example without the shear flow ($u_w = 0$) where four partial spreading cases (a)–(d) and two total spreading cases (e)–(f) are simulated.

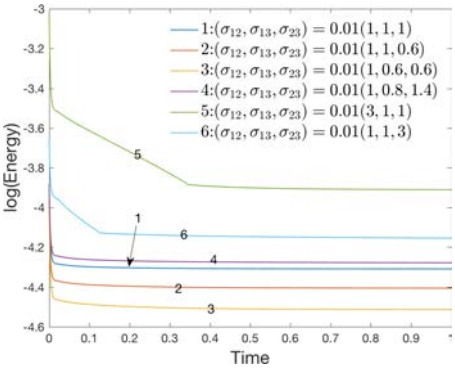

(a) Log(Energy) evolution.

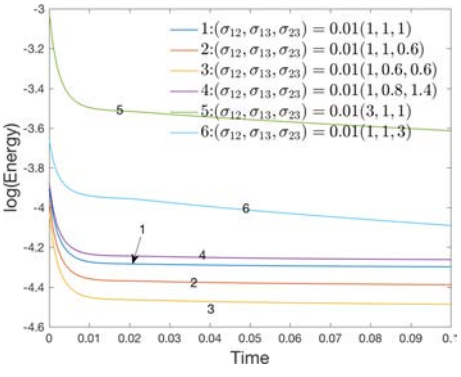

(b) A close-up view where the energies decay fast.

Fig. 9. Time evolution of the logarithm of the total free energy (3.51) for the spinodal decomposition examples without the shear flow ($u_w = 0$) where various surface tension parameters are used.

$(\sigma_{12}, \sigma_{13}, \sigma_{23}) = 0.01(3, 1, 1)$. These theoretical predictions for contact angles are all verified by the computed results shown by the equilibrium solutions plotted in each final subfigure of Figs. 8(a)–8(f). In Fig. 10, for the above three partial spreading cases, we compare the equilibrium solutions calculated using the original ternary Cahn–Hilliard model[2,4] and the provided nonlinear schemes with $\delta t = 1e-5$, and the new volume-conserved Allen–Cahn model with the new developed scheme with $\delta t = 1e-3$. We note that there are almost no viewable differences between the obtained contact angles, which illustrates the effectiveness of the new model and the robustness of the algorithm. In Fig. 9, we plot the time evolution of the total free energy for all simulated cases.

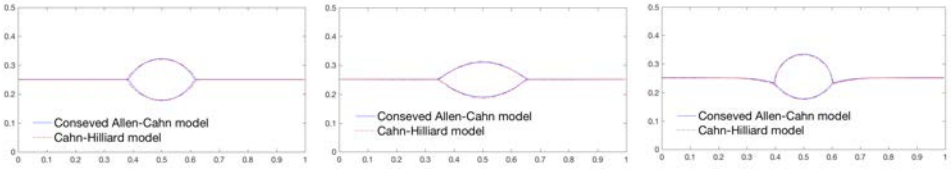

Fig. 10. Comparison of equilibrium solutions of three partial spreading cases calculated using the conserved ternary Allen–Cahn model (2.13)–(2.16) and the ternary Cahn–Hilliard model computed by the nonlinear scheme provided in Refs. 2 and 4 with $\delta t = 1e-5$. From left to right are $(\sigma_{12}, \sigma_{13}, \sigma_{23}) = 0.01(1, 1, 1)$, $0.01(1, 0.6, 0.6)$, and $0.01(1, 0.8, 1.4)$, respectively.

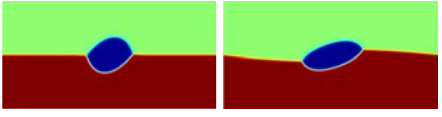

(a) $t = 0.2, 10$ with $(\sigma_{12}, \sigma_{13}, \sigma_{23}) = 0.01(1, 1, 1)$.

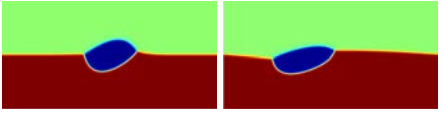

(b) $t = 0.4, 6$ with $(\sigma_{12}, \sigma_{13}, \sigma_{23}) = 0.01(1, 1, 0.6)$.

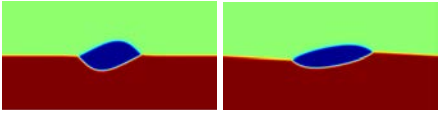

(c) $t = 0.4, 6$ with $(\sigma_{12}, \sigma_{13}, \sigma_{23}) = 0.01(1, 0.6, 0.6)$.

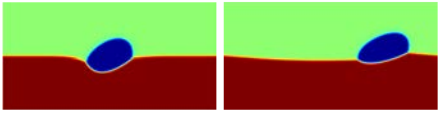

(d) $t = 0.4, 6$ with $(\sigma_{12}, \sigma_{13}, \sigma_{23}) = 0.01(1, 0.8, 1.4)$.

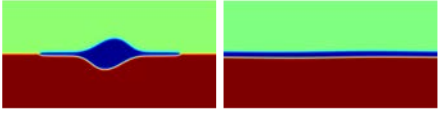

(e) $t = 0.2, 3$ with $(\sigma_{12}, \sigma_{13}, \sigma_{23}) = 0.01(3, 1, 1)$.

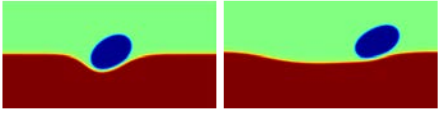

(f) $t = 0.4, 3$ with $(\sigma_{12}, \sigma_{13}, \sigma_{23}) = 0.01(1, 1, 3)$.

Fig. 11. The 2D dynamical evolution of the profile $\frac{1}{2}\phi_1 + \phi_2$ for the liquid lens example with the shear flow ($u_w = 0.5$) where four partial spreading cases (a)–(d) and two total spreading cases (e)–(f) are simulated.

Furthermore, we impose the shear flow on the wall with $u_w = 0.5$ and plot the snapshots of the profile $\frac{1}{2}\phi_1 + \phi_2$ at various times in Figs. 11(a)–11(f). We observe that liquid lens is deformed by the flow field while the contact angles for each phase are still consistent with the no shear cases that follow Young's relation as well.

4.5. *The dynamics of a rising liquid drop with various surface tensions and gravity forces*

In this example, we investigate how a liquid bubble rises and deforms across a liquid/liquid interface driven by the gravity force. We consider the case where the density difference of the liquid crystal drop and ambient fluid is small so that we can use the Boussinesq approximation (see also Refs. 26 and 33) and replace the momentum equation as follows:

$$\mathbf{u}_t + \mathbf{u}\cdot\nabla\mathbf{u} - \nu\Delta\mathbf{u} + \nabla p - \sum_{i=1}^{3}\bar{\mu}_i\nabla\phi_i + \sum_{i=1}^{3}\nabla(\phi_i\bar{\mu}_i) = \mathbf{g}_0\phi_3, \tag{4.6}$$

with $\mathbf{g}_0 = (0, g_0)$ for 2D and $\mathbf{g}_0 = (0, 0, g_0)$ for 3D where g_0 is the pre-assumed gravity constant.

We first perform 2D simulations and set the computational domain as $(x, y) \in \Omega = [0, 1] \times [0, 2]$. The periodic boundary conditions are set for the x-axis and we discretize it using 257 Fourier modes. For the y-axis, we adopt the boundary conditions given in (3.18) and (3.21) and discretize it by using Legendre polynomials up to the degree of 512. The initial conditions for variables ϕ_i (sketches of the profiles shown in Fig. 12(a)), $\mathbf{u}$, and p are set as follows:

$$\begin{aligned}
&\phi_1^0(x, y) = (1 - \phi_3^0)\left(\frac{1}{2} + \frac{1}{2}\tanh\left(\frac{5}{\epsilon}(y - 1)\right)\right),\\
&\phi_2^0(x, y) = 1 - \phi_1^0 - \phi_3^0,\\
&\phi_3^0(x, y) = \frac{1}{2}\tanh\left(\frac{0.15 - \sqrt{(x - 0.5)^2 + (y - 0.6)^2}}{\epsilon/5}\right) + \frac{1}{2},\\
&\mathbf{u}^0(x, y) = (0, 0), \quad p^0(x, y) = 0.
\end{aligned} \tag{4.7}$$

We also set $\delta t = 0.01$, $\nu = 1$, $\epsilon = 0.028$, $M = \frac{1}{\epsilon}$, $B = 10$, and $S = 10$. We vary the surface tension parameters $(\sigma_{12}, \sigma_{13}, \sigma_{23})$ and the gravity parameter g_0 to investigate how the liquid bubble evolves with time.

In Fig. 13, we set the surface tension parameter as $(\sigma_{12}, \sigma_{13}, \sigma_{23}) = 0.01(1, 1, 1)$ and use two different gravity parameters $g_0 = 10$ and 20. With the weak gravity constant $g_0 = 10$, snapshots of $\frac{1}{2}\phi_1 + \phi_2$ shown in Fig. 13(a), the liquid bubble penetrates the liquid/liquid interface and remains captured between the two liquid layers. We also note the three equal contact angles are formed due to three equal surface tension parameters. For comparison, with the strong gravity constant $g_0 = 20$, snapshots of $\frac{1}{2}\phi_1 + \phi_2$ shown in Fig. 13(b), the liquid bubble finally rises into the upper liquid after penetrating the interface.

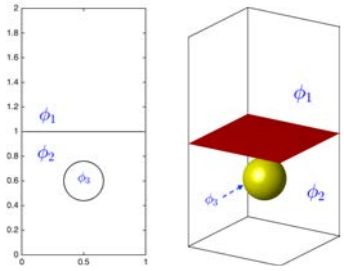

(a) 2D. (b) 3D.

Fig. 12. The 2D and 3D initial profiles of the rising fluid bubble example.

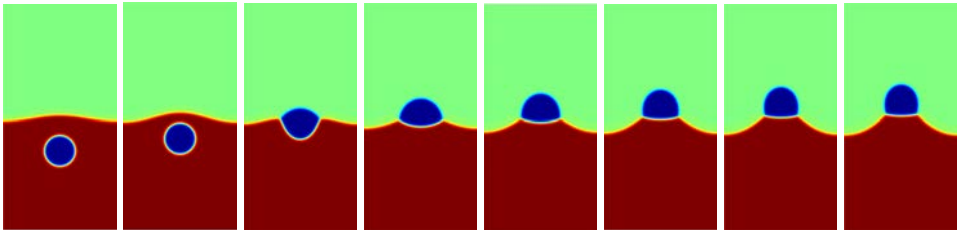

(a) $g_0 = 20$ with snapshots taken at $t = 1.2$, 2.4, 3.6, 4.8, 6, 7.2, 8.4, and 9.6.

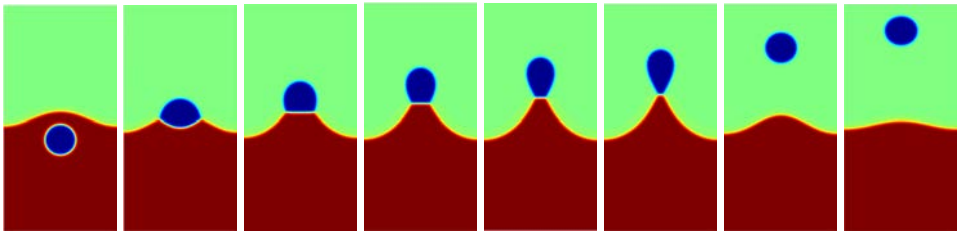

(b) $g_0 = 30$ with snapshots taken at $t = 1.2$, 2.4, 3.6, 4.8, 6, 7.2, 8.4, and 9.6.

Fig. 13. The 2D dynamical evolution of the profile $\frac{1}{2}\phi_1 + \phi_2$ for rising bubble examples with $(\sigma_{12}, \sigma_{13}, \sigma_{23}) = 0.01(1, 1, 1)$ and various gravity parameters $g_0 = 10$ and $g_0 = 20$.

Furthermore, we change the surface tension parameter to $(\sigma_{12}, \sigma_{13}, \sigma_{23}) = 0.01(1, 0.6, 0.6)$ and use two different gravity parameters $g_0 = 10$ and 120 as well. We get very similar phenomena that the small gravity parameter induces that the liquid bubble is captured by the liquid layer and the large gravity parameter leads to the interface penetration of the liquid bubble from the lower liquid to the upper liquid.

Finally, we perform simulations in 3D and set the computational domain as $\Omega = [0, 1] \times [0, 1] \times [0, 2]$. Similar to the 2D simulations, we set the periodic boundary conditions for the x and y-axes and discretize it using 129^2 Fourier modes. The z-direction is equipped with the physical boundary conditions given in (3.18) and

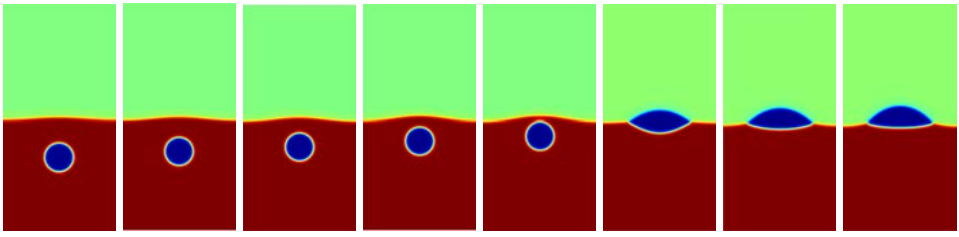

(a) $g_0 = 10$ with snapshots taken at $t = 1.2$, 2.4, 3.6, 4.8, 6, 7.2, 8.4, and 9.6.

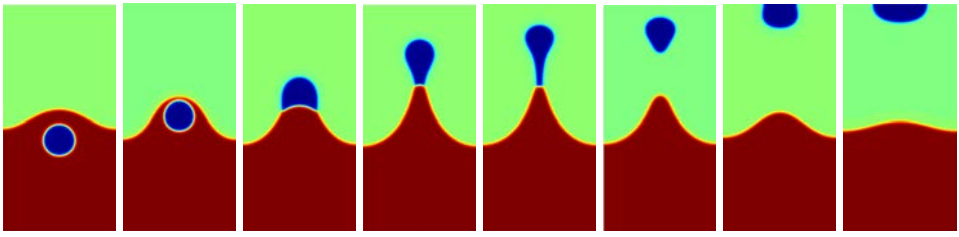

(b) $g_0 = 120$ with snapshots taken at $t = 0.4$, 0.8, 1.2, 2, 2.4, 2.8, 3.6, and 4.8.

Fig. 14. The 2D dynamical evolution of the profile $\frac{1}{2}\phi_1 + \phi_2$ for rising bubble examples with $(\sigma_{12}, \sigma_{13}, \sigma_{23}) = 0.01(1, 0.6, 0.6)$ and various gravity parameters $g_0 = 10$ and $g_0 = 120$.

(3.21) and it is discretized by using Legendre polynomials up to the degree of 256. The initial conditions are set as follows:

$$\begin{aligned}
&\phi_1^0(x,y,z) = (1-\phi_3^0)\left(\frac{1}{2} + \frac{1}{2}\tanh\left(\frac{5}{\epsilon}(z-1)\right)\right),\\
&\phi_2^0(x,y,z) = 1 - \phi_1^0 - \phi_3^0,\\
&\phi_3^0(x,y,z) = \frac{1}{2}\tanh\left(\frac{0.15 - \sqrt{(x-0.5)^2 + (y-0.5)^2 + (z-0.6)^2}}{\epsilon/5}\right) + \frac{1}{2},\\
&\mathbf{u}^0(x,y,z) = (0,0,0), \quad p^0(x,y,z) = 0.
\end{aligned} \tag{4.8}$$

The initial condition for the phase-field variables ϕ_i are sketched in Fig. 12(b) and the other parameters are set as $\delta t = 0.01$, $\nu = 1$, $\epsilon = 0.028$, $M = \frac{1}{\epsilon}$, $B = 10$, and $S = 10$. In Figs. 15(a) and 15(b) and Figs. 16(a) and 16(b), for the computed results, we plot the isosurfaces of $\{\phi_1 = \frac{1}{2}\}$ and $\{\phi_2 = \frac{1}{2}\}$ using different colors by varying the gravity parameters and the surface tension parameters, i.e. $(\sigma_{12}, \sigma_{13}, \sigma_{23}) = 0.01(1, 1, 1)$ with $g_0 = 10$ in Fig. 15(a); $(\sigma_{12}, \sigma_{13}, \sigma_{23}) = 0.01(1, 1, 1)$ with $g_0 = 20$ in Fig. 15(b); $(\sigma_{12}, \sigma_{13}, \sigma_{23}) = 0.01(1, 0.6, 0.6)$ with $g_0 = 10$ in Fig. 16(a); and $(\sigma_{12}, \sigma_{13}, \sigma_{23}) = 0.01(1, 0.6, 0.6)$ with $g_0 = 120$ in Fig. 16(b). The simulations are consistent to the 2D results and the similar two behaviors occur, i.e. the capturing in the layer and rising to the upper fluid.

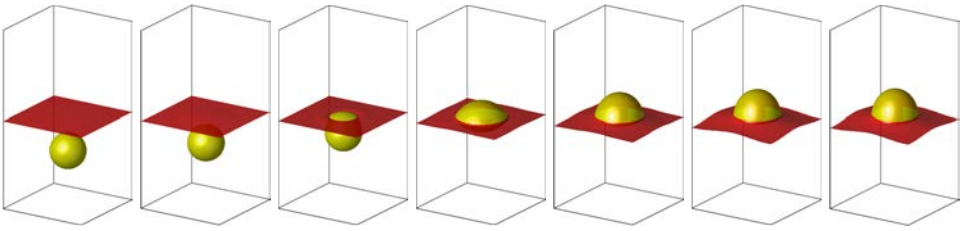

(a) $g_0 = 10$ with snapshots taken at $t = 0.2$, 1.8, 3.8, 5.8, 9, 17, and 30.

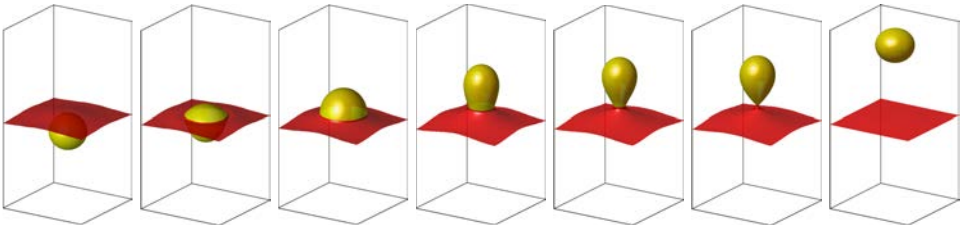

(b) $g_0 = 20$ with snapshots taken at $t = 2.2$, 3, 5, 11, 13.4, 13.8, and 17.8.

Fig. 15. The 3D dynamical evolution of the isosurfaces $\{\phi_1 = \frac{1}{2}\}$ and $\{\phi_3 = \frac{1}{2}\}$ for rising bubble examples with $(\sigma_{12}, \sigma_{13}, \sigma_{23}) = 0.01(1, 1, 1)$ and various gravity parameters $g_0 = 10$ and $g_0 = 20$.

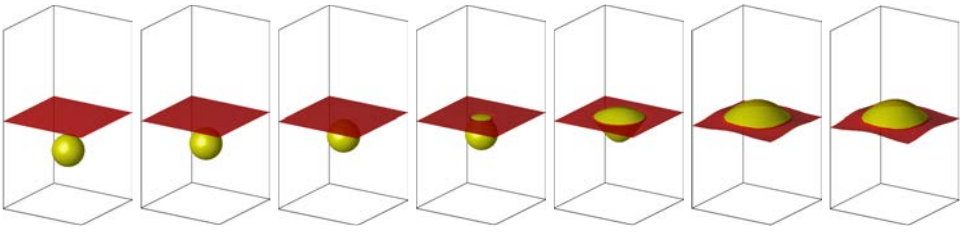

(a) $g_0 = 10$ with snapshots taken at $t = 0.2$, 3.4, 3.8, 4.2, 5, 9, and 16.2.

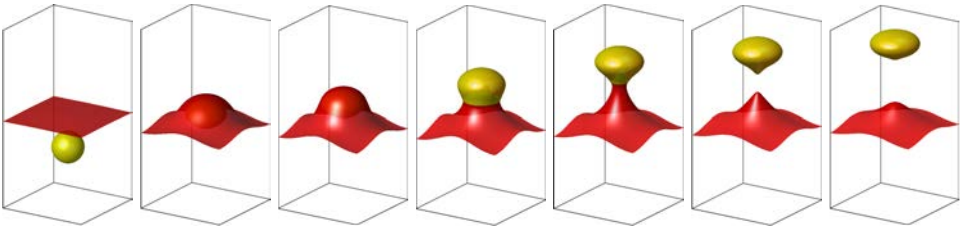

(b) $g_0 = 120$ with snapshots taken at $t = 0.2$, 1.4, 1.8, 2.6, 3.4, 3.8, and 4.2.

Fig. 16. The 3D dynamical evolution of the isosurfaces $\{\phi_1 = \frac{1}{2}\}$ and $\{\phi_3 = \frac{1}{2}\}$ for rising bubble examples with $(\sigma_{12}, \sigma_{13}, \sigma_{23}) = 0.01(1, 0.6, 0.6)$ and various gravity parameters $g_0 = 10$ and $g_0 = 120$.

5. Concluding Remarks

In this paper, we develop a new hydrodynamically coupled phase-field model for three immiscible fluid components system and construct an efficient scheme to solve the model. The scheme combines the recently developed IEQ approach with the stabilization technique, the projection method, as well as the implicit–explicit treatments for the nonlinear stress and convective terms. The well-posedness of the scheme and its unconditional energy stability are rigorously proved. We demonstrate the effectiveness of the new model, as well as the stability and the accuracy of the developed scheme in simulating numerous numerical examples of 2D and 3D including the spinodal decomposition, contact lens, and rising bubbles.

Acknowledgment

X. Yang was partially supported by National Science Foundation with Grant Numbers DMS-1720212, DMS-1818783, and DMS-2012490.

References

1. D. M. Anderson, G. B. McFadden and A. A. Wheeler, Diffuse-interface methods in fluid mechanics, *Annu. Rev. Fluid Mech.* **30** (1998) 139–165.
2. F. Boyer and C. Lapuerta, Study of a three component Cahn–Hilliard flow model, *ESAIM*: *Math. Model. Numer. Anal.* **40** (2006) 653–687.
3. F. Boyer, C. Lapuerta, S. Minjeaud, B. Piar and M. Quintard, Cahn–Hilliard/Navier–Stokes model for the simulation of three-phase flows, *Transp. Porous Media* **82** (2010) 463–483.
4. F. Boyer and S. Minjeaud, Numerical schemes for a three component Cahn–Hilliard model, *ESAIM*: *Math. Model. Numer. Anal.* **45** (2011) 697–738.
5. C. Chen and X. Yang, Efficient numerical scheme for a dendritic solidification phase field model with melt convection, *J. Comput. Phys.* **388** (2019) 41–62.
6. C. Chen and X. Yang, Fast, provably unconditionally energy stable, and second-order accurate algorithms for the anisotropic Cahn–Hilliard model, *Comput. Meth. Appl. Mech. Eng.* **351** (2019) 35–59.
7. A. Christlieb, J. Jones, K. Promislow, B. Wetton and M. Willoughby, High accuracy solutions to energy gradient flows from material science models, *J. Comput. Phys.* **257** (2014) 192–215.
8. C. M. Elliott and H. Garcke, Diffusional phase transitions in multicomponent systems with a concentration dependent mobility matrix, *Physica D* **109** (1997) 242–256.
9. D. J. Eyre, Unconditionally gradient stable time marching the Cahn–Hilliard equation, in *Computational and Mathematical Models of Microstructural Evolution*, *Materials Research Society Symposium Proceedings*, Vol. 529 (Cambridge Univ. Press, 1998), pp. 39–46.
10. X. Feng and A. Prohl, Numerical analysis of the Allen–Cahn equation and approximation for mean curvature flows, *Numer. Math.* **94** (2003) 33–65.
11. X. Feng, Y. He and C. Liu, Analysis of finite element approximations of a phase field model for two-phase fluids, *Math. Comp.* **76** (2007) 539–571 (electronic).
12. M. E. Gurtin, D. Polignone and J. Viñals, Two-phase binary fluids and immiscible fluids described by an order parameter, *Math. Models Methods Appl. Sci.* **6** (1996) 815–831.

13. D. Jacqmin, Calculation of two-phase Navier–Stokes flows using phase-field modeling, *J. Comput. Phys.* **155** (1999) 96–127.
14. J. Kim, Phase-field models for multi-component fluid flows, *Commun. Comput. Phys.* **12** (2012) 613–661.
15. J. Kim, K. Kang and J. Lowengrub, Conservative multigrid methods for ternary Cahn–Hilliard systems, *Commun. Math. Sci.* **2** (2004) 53–77.
16. J. Kim and J. Lowengrub, Phase field modeling and simulation of three-phase flows, *Interface Free Bound.* **7** (2005) 435–466.
17. T. S. Little, V. Mironov, A. Nagy-Mehesz, R. Markwald, Y. Sugi, S. M. Lessner, M. A. Sutton, X. Liu, Q. Wang, X. Yang, J. O. Blanchette and M. Skiles, Engineering a 3D, biological construct: Representative research in the south carolina project for organ biofabrication, *Biofabrication* **3** (2011) 030202.
18. C. Liu and J. Shen, A phase field model for the mixture of two incompressible fluids and its approximation by a Fourier-spectral method, *Physica D* **179** (2003) 211–228.
19. J. Lowengrub, A. Ratz and A. Voigt, Phase field modeling of the dynamics of multicomponent vesicles spinodal decomposition coarsening budding and fission, *Phys. Rev. E* **79** (2009) 031926.
20. J. Lowengrub and L. Truskinovsky, Quasi-incompressible Cahn–Hilliard fluids and topological transitions. *Proc. R. Soc. Lond. Proc. Ser. A Math. Phys. Eng. Sci.* **454** (1998) 2617–2654.
21. L. Ma, R. Chen, X. Yang and H. Zhang, Numerical approximations for Allen–Cahn type phase field model of two-phase incompressible fluids with moving contact lines, *Comm. Comput. Phys.* **21** (2017) 867–889.
22. C. Miehe, M. Hofacker and F. Welschinger, A phase field model for rate-independent crack propagation: Robust algorithmic implementation based on operator splits, *Comput. Methods Appl. Mech. Eng.* **199** (2010) 2765–2778.
23. S. Minjeaud, An unconditionally stable uncoupled scheme for a triphasic Cahn–Hilliard/Navier–Stokes model, *Numer. Methods Partial Differ. Equ.* **29** (2013) 584–618.
24. J. S. Rowlinson and B. Widom, *Molecular Theory of Capillarity* (Clarendon Press, 1989).
25. J. Shen and X. Yang, Numerical approximations of Allen–Cahn and Cahn–Hilliard equations, *Disc. Cont. Dyn. Syst. A* **28** (2010) 1669–1691.
26. J. Shen and X. Yang, Decoupled energy stable schemes for phase filed models of two phase complex fluids, *SIAM J. Sci. Comput.* **36** (2014) B122–B145.
27. J. Shen and X. Yang, The IEQ and SAV approaches and their extensions for a class of highly nonlinear gradient flow systems, *Contemp. Math.* **754** (2020) 217–245.
28. X. Yang, Linear, first and second order and unconditionally energy stable numerical schemes for the phase field model of homopolymer blends, *J. Comput. Phys.* **327** (2016) 294–316.
29. X. Yang, Efficient Linear, stabilized, second-order time marching schemes for an anisotropic phase field dendritic crystal growth model, *Comput. Meth. Appl. Mech. Eng.* **347** (2019) 316–339.
30. X. Yang, A novel fully-decoupled scheme with second-order time accuracy and unconditional energy stability for the Navier–Stokes equations coupled with mass-conserved Allen–Cahn phase-field model of two-phase incompressible flow, *Int. J. Numer. Methods Eng.* **122** (2021) 1283–1306.
31. X. Yang, A novel fully-decoupled, second-order and energy stable numerical scheme of the conserved Allen–Cahn type flow-coupled binary surfactant model, *Comput. Methods Appl. Mech. Eng.* **373** (2021) 113502.

32. X. Yang, Numerical approximations of the Navier–Stokes equation coupled with volume-conserved multi-phase-field vesicles system: Fully-decoupled, linear, unconditionally energy stable and second-order time-accurate numerical scheme, *Comput. Methods Appl. Mech. Eng.* **375** (2021) 113600.
33. X. Yang, J. J. Feng, C. Liu and J. Shen, Numerical simulations of jet pinching-off and drop formation using an energetic variational phase-field method, *J. Comput. Phys.* **218** (2006) 417–428.
34. X. Yang, G. Forest, C. Liu and J. Shen, Shear cell rupture of nematic droplets in viscous fluids, *J. Non-Newtonian Fluid Mech.* **166** (2011) 487–499.
35. X. Yang and H. Yu, Efficient second-order unconditionally stable schemes for a phase field moving contact line model using an invariant energy quadratization approach, *SIAM J. Sci. Comput.* **40** (2018) B889–B914.
36. X. Yang, J. Zhao, Q. Wang and J. Shen, Numerical approximations for a three components Cahn–Hilliard phase-field model based on the invariant energy quadratization method, *M3AS*: *Mathematical Models Methods Appl. Sci.* **27** (2017) 1993–2030.
37. J. Zhang, C. Chen and X. Yang, A novel decoupled and stable scheme for an anisotropic phase-field dendritic crystal growth model, *Appl. Math Lett.* **95** (2019) 122–129.
38. J. Zhang and X. Yang, Decoupled, non-iterative, and unconditionally energy stable large time stepping method for the three-phase Cahn–Hilliard phase-field model, *J. Comput. Phys.* **404** (2020) 109115.
39. J. Zhang and X. Yang, Unconditionally energy stable large time stepping method for the L2-gradient flow based ternary phase-field model with precise nonlocal volume conservation, *Comput. Methods Appl. Mech. Eng.* **361** (2020) 112743.